Dissociable Roles of Pallidal Neuron Subtypes in Regulating Motor Patterns

Suraj Cherian[1*], Qiaoling Cui[1*], Arin Pamukcu[1*], Isaac Y. M. Chang[1*], Brianna L. Berceau[1], Harry S. Xenias[1], Mathew H. Higgs[2], Shivakumar Rajamanickam[3,4], Yi Chen[5], Xixun Du[1], Yu Zhang[1], Hayley McMorrow[1], Zachary A. Abecassis[1], Simina M. Boca[6], Nicholas J. Justice[3,4], Charles J. Wilson[2], C. Savio Chan[1]

[1] Department of Physiology, Feinberg School of Medicine, Northwestern University, Chicago, IL, USA
[2] Department of Biology, University of Texas at San Antonio, San Antonio, TX, USA
[3] Center for Metabolic and degenerative disease, Institute of Molecular Medicine, University of Texas, Houston, TX, USA
[4] Department of Integrative Pharmacology, University of Texas, Houston, TX, USA
[5] Department of Biostatistics and Medical Informatics, University of Wisconsin-Madison, Madison, WI, USA
[6] Innovation Center for Biomedical Informatics, Georgetown University Medical Center, Washington D.C., USA

*These authors contributed equally to this work.

Correspondence should be addressed to C. Savio Chan, Department of Physiology, Feinberg School of Medicine, Northwestern University, 303 East Chicago Avenue, Chicago, IL 60611. saviochan@gmail.com

Running title: GPe neurons control motor patterns

Acknowledgments

We thank Daniela Garcia, Alyssa Bebenek, Moises Melesio, Kris Shah, Ahana Narayanan, Vaishnavi Tetali, Saivasudha Chalasani, and Daniel Hegeman for their assistance on the project, Dr. Tiffany Schmidt for providing Kcng4-Cre mice, Dr. Byung Kook Lim for providing the synaptophysin-GFP virus, and Drs. Ann Kennedy and Sam Golden for input on the behavioral analyses. This work is supported by NIH R01 NS069777 (CSC), R01 MH112768 (CSC), R01 NS097901 (CSC), R01 MH109466 (CSC), R01 NS088528 (CSC), T32 AG020506 (AP), T32 NS041234 (HSX), F32 NS098793 (HSX), R01 MH112768 (NJJ), R35 NS097185 (CJW), HHMI-PF Medical Research Fellowship (ZAA), and AΩA Student Research Fellowship (ZAA).

Author contributions

SC and BLB performed histological analysis. SC, QC, IYMC, HSX, YZ, HM, ZAA, and XD surveyed the intrinsic properties. QC, HMH, XD, YZ, and CJW examined the local connectivity. AP, QC, SR, and NJJ conducted the behavioral studies. IYMC developed the machine learning analysis pipeline. YC and SMB provided expertise for neuron classification. CSC wrote the manuscript with input from all co-authors. All authors reviewed and edited the manuscript. CSC designed, directed, and supervised the project.

Abstract (225 words)

We have previously established that PV$^+$ neurons and Npas1$^+$ neurons are distinct neuron classes in the GPe—they have different topographical, electrophysiological, circuit, and functional properties. Aside from Foxp2$^+$ neurons, which are a unique subclass within the Npas1$^+$ class, we lack driver lines that effectively capture other GPe neuron subclasses. In this study, we examined the utility of Kcng4-Cre, Npr3-Cre, and Npy2r-Cre mouse lines (both males and females) for the delineation of GPe neuron subtypes. By using these novel driver lines, we have provided the most exhaustive investigation of electrophysiological studies of GPe neuron subtypes to date. Corroborating our prior studies, GPe neurons can be divided into two statistically distinct clusters that map onto PV$^+$ and Npas1$^+$ classes. By combining optogenetics, and machine learning-based tracking, we showed that optogenetic perturbation of GPe neuron subtypes generated unique behavioral structures. Our findings further highlighted the dissociable roles of GPe neurons in regulating movement and anxiety. We concluded that Npr3$^+$ neurons and Kcng4$^+$ neurons are distinct subclasses of Npas1$^+$ neurons and PV$^+$ neurons, respectively. Finally, by examining local collateral connectivity, we inferred the circuit mechanisms involved in the motor patterns observed with optogenetic perturbations. In summary, by identifying mouse lines that allow for manipulations of GPe neuron subtypes, we created new opportunities for interrogations of cellular and circuit substrates that can be important for motor function and dysfunction.

Significance statement (102 words)

Within the basal ganglia, the external globus pallidus (GPe) has long been recognized for its involvement in motor control. However, we lacked an understanding of precisely how movement is controlled at the GPe level as a result of its cellular complexity. In this study, by using transgenic and cell-specific approaches, we showed that genetically-defined GPe neuron subtypes have distinct roles in regulating motor patterns. In addition, the *in vivo* contributions of these neuron subtypes are in part shaped by the local, inhibitory connections within the GPe. In sum, we have established the foundation for future investigations of motor function and disease pathophysiology.

Introduction (484 words)

The basal ganglia are a network of subcortical structures that are involved in motor control and adaptive behavior. Dysfunction within this circuit can be devastating, as seen in patients afflicted with Parkinson's disease (PD) (Albin et al., 1989; DeLong, 1990; Graybiel et al., 1994; Mink, 1996; DeLong and Wichmann, 2007; Redgrave et al., 2010; Nelson and Kreitzer, 2014; Jahanshahi et al., 2015; Dudman and Krakauer, 2016; Grillner and Robertson, 2016; Klaus et al., 2019; Park et al., 2020). The external globus pallidus (GPe) is reciprocally connected with the dorsal striatum (dStr) and subthalamic nucleus (STN) and is expected to regulate motor output (Smith et al., 1998; Kita, 2007; Hernandez et al., 2015; Glajch et al., 2016; Hegeman et al., 2016; Pamukcu et al., 2020). Consistent with this idea, decorrelated, phasic changes in GPe neuron activity are observed with normal movements (Anderson and Horak, 1985; Shi et al., 2004; Turner and Anderson, 2005; Jin et al., 2014; Dodson et al., 2015; Mallet et al., 2016). Alterations in the firing pattern of these neurons are associated with hypokinetic motor symptoms in both animal models of PD and human patients (Filion et al., 1991; Hutchison et al., 1994; Nini et al., 1995; Rothblat and Schneider, 1995; Boraud et al., 1998; Raz et al., 2000; Magill et al., 2001; Mallet et al., 2008; Chan et al., 2011; Jaeger and Kita, 2011).

Although the importance of the GPe has long been recognized, our understanding of its cell types, their organization, and their functional properties is limited. While prior studies have suggested GPe neurons are involved in movement control (Dodson et al., 2015; Glajch et al., 2016; Mastro et al., 2017), precisely how they are involved in motor function and dysfunction remains poorly defined. A major hurdle has been imposed by the complexity of the cellular makeup of the GPe. Our past work characterized two principal classes of GPe neurons, parvalbumin-expressing (PV^+) neurons and Npas1-expressing ($Npas1^+$) neurons that account for roughly 50% and 30% of the GPe, respectively (Hernandez et al., 2015; Hegeman et al., 2016; Abecassis et al., 2020). Aside from Foxp2-expressing ($Foxp2^+$) neurons that form a unique subclass within the $Npas1^+$ class, we lack driver lines that selectively capture other GPe neuron subclasses. The advent of transcriptomic data provided key insights for genetic dissection of GPe neuron subtypes. In particular, pre-existing single-cell transcriptomic studies (Saunders et al., 2018) and *in situ* hybridization data suggest the existence of molecular markers that can be utilized but have not been previously explored for the interrogation of GPe neuron subtypes. Here, we examined the utility of Kcng4-Cre, Npr3-Cre, and Npy2r-Cre mouse lines in this study. Using complementary approaches, such as anatomical,

electrophysiological, and behavioral approaches, we concluded that Npr3^{+} neurons and Kcng4^{+} neurons are unique neuron subclasses within the GPe. Critically, capitalizing on newly available transgenic tools, we showed that GPe neuron subtypes were distinct in their roles in regulating motor patterns.

Methods (3185 words)

Mice

All procedures were done in accordance with protocols approved by Northwestern University and The University of Texas Health Science Center at Houston Institutional Animal Care and Use Committees and were in compliance with the National Institutes of Health Guide to the Care and Use of Laboratory Animals. Experiments were conducted with the following mouse lines: Adora2a-Cre BAC (A2a-Cre, MMRRC 031168), C57BL/6J (C57, Jax 000664), Drd1a-Cre BAC (D1-Cre, MMRRC 029178), Foxp2-ires-Cre (Foxp2-Cre, Jax 030541), FSF(Frt-STOP-Frt)-LSL-tdTomato (Ai65, Jax 021875), Kcng4-Cre (Jax 029414), Lox-STOP-Lox(LSL)-tdTom (Ai14, Jax 007914), Npr3-ires2-Cre (Npr3-Cre, Jax 031333), Npy2r-ires-Cre (Npy2r-Cre, Jax 029285), Npas1-Cre-tdTomato BAC (Npas1-Cre, Jax 027718), PV-ires-Cre (PV-Cre, Jax 017320), PV-2A-Flp (PV-Flp , Jax 022730), PV-tdTomato BAC (PV-tdTom, Jax 027395). To genetically label different neuron populations for histological and electrophysiological studies, the following crosses were made: Foxp2-Cre;PV-tdTom (Foxp2-PV), Npr3-Cre;Ai14 (Npr3-L-tdTom), Npy2r-Cre;Ai14 (Npy2r-L-tdTom), PV-Flp;Npy2r-Cre;Ai65 (PV-Npy2r-FL-tdTom), PV-Cre;Ai14 (PV-L-tdTom), PV-tdTom;Lhx6-eGFP (PV-Lhx6), Npas1-Cre;Lhx6-eGFP (Npas1-Lhx6), and Npas1-Cre;PV-tdTom (Npas1-PV). Only heterozygous and hemizygous mice were used throughout the study to minimize the potential alteration of the phenotypes in mice carrying the transgene alleles (Chan et al., 2012). All mouse lines were maintained by backcrossing with C57BL/6J stock. Mice were group-housed in a 12 h light-dark cycle. Food and water were provided *ad libitum*. The genotypes of all transgenic mice were determined by tail biopsy followed by PCR to identify the presence of the relevant transgenes. Both male and female mice were used in this study.

Immunolabeling and biocytin visualization

Mice ranging in age from postnatal day 55–80 were anesthetized deeply with a ketamine-xylazine mixture and perfused transcardially first with phosphate-buffered saline (PBS) followed by a fixative containing 4% (w/v) paraformaldehyde (PFA, pH 7.4). Tissue was then postfixed in the same fixative for 2 h at 4 ºC. Tissue blocks containing the GPe were sectioned using a vibrating microtome (Leica Instruments) at a thickness of 60 μm. Floating sections were blocked with 10% (v/v) normal goat or donkey serum (Thermo Fisher Scientific) and 0.2% (v/v) Triton X-100 in PBS for 30–60 min, and were subsequently incubated with primary antibodies in the same solution for 16–24 h at 4 ºC. Details of the primary antibodies used in this study can be found in our recent publication (Abecassis et al., 2020). After washes in PBS, the sections were incubated with Alexa-conjugated secondary antibodies (Thermo Fisher Scientific, 1:500 dilution) at room temperature for 2 h. The sections were then washed, mounted with ProLong Antifade mounting medium (Thermo Fisher Scientific), and coverslipped. In a subset of the experiments, DAPI was used to delineate cytoarchitecture of different brain structures. Fluorescent images of injection sites were captured on an epifluorescence microscope (Keyence Corporation) using a 2× or 10× 0.45 numerical aperture (NA) objective. Immunoreactivity in neurons was examined on a laser-scanning confocal microscope (Olympus). For cell quantification, images of the entire GPe were acquired on a laser-scanning confocal microscope with a 60× 1.35 NA oil-immersion objective. Images encompassing the GPe were taken and stitched using FLUOVIEW Viewer (Olympus) or Photoshop (Adobe Systems). Cell counting was performed manually using the cell-counter plugin within Fiji (Schindelin et al., 2012). Cell counts were obtained from optical sections that were captured at 1 μm increments. Neurons were defined by cells that were immuno-positive for HuCD or NeuN (Hernandez et al., 2015; Abecassis et al., 2020). GPe sections from three different equally-spaced (400 μm) lateromedial levels (~2.5, 2.1, and 1.7 mm from bregma) were sampled and assigned as lateral, intermediate, and medial, respectively (Hernandez et al., 2015; Abecassis et al., 2020). They correspond approximately to sagittal plate 7, 9, and 11 on the Allen reference atlas (http://mouse.brain-map.org/static/atlas). In this study, the GPe is considered to be the structure that spans between the dorsal striatum and the internal capsule, which define the rostral and caudal borders of the GPe on a sagittal plane, respectively. The cytoarchitecture of the ventral border is more ambiguous. For consistency, six non-overlapping z-stacks (212.13 × 212.13 μm) traversing the long axis of the GPe were used to capture its dorsoventral extent.

To visualize biocytin GPe neurons, 0.2% (w/v) biocytin was included in the internal solution and recorded in the whole-cell mode for at least 30 minutes (see below). Recovered slices were flat-mounted on nitrocellulose filters (Millipore) and fixed overnight in 4% (w/v) paraformaldehyde (PFA, pH 7.4) at 4 ºC. After several washes in PBS, slices were reacted three times in freshly prepared 0.5% (w/v) $NaBH_4$ in H_2O. Slices were then incubated in fresh Scale (Hama et al., 2011) solution (4 M urea, 10% (v/v) glycerol and 0.1% Triton X-100) for 10 days at 4 ºC. Subsequently, slices were washed in PBST (1% Triton X-100 in PBS) and blocked in 10% (v/v) normal goat serum and PBST for 45 min. After several washes, slices were reacted with 2 µg/ml streptavidin-Alexa Fluor 647 (Thermo Fisher Scientific) in blocking solution overnight at 4 ºC in the dark. Slices were washed in PBS followed by Scale solution. Sections were mounted, air-dried, and then coverslipped in ProLong Gold mounting medium (Thermo Fisher Scientific). Serial optical sections (Z-stacks) were acquired on a laser-scanning confocal microscope (Olympus) with a 60× 1.35 NA oil-immersion objective (Olympus) at 1 µm intervals and stitched together using Fiji.

Stereotaxic injections and fiber implantations

For *in vivo* optogenetic experiments, mice aged postnatal day 28–35 were anesthetized in an isoflurane induction chamber at 3–4% isoflurane and immobilized on a stereotaxic frame (David Kopf Instruments). Anesthesia was maintained using 1–2% isoflurane. The scalp was opened using a scalpel and a small craniotomy (1 mm diameter) was made with a dental drill (Osada). Adeno-associated viruses (AAVs) were infused with calibrated 5 µl glass pipettes (VWR) pulled to have a tip diameter of 3 µm. The injection needle was left *in situ* for 5–10 min following the end of the injection to maximize tissue retention of AAV and decrease capillary spread upon pipette withdrawal. Experiments were performed 4–6 weeks after stereotaxic surgeries. The accuracy of injections was visually inspected under epifluorescence microscopy in *ex vivo* slices or histologically verified *post hoc*.

To allow for optogenetic manipulations, fiber optic cannulae were implanted bilaterally at the region of interest (Pamukcu et al., 2020) three weeks after stereotaxic injections. Each fiber cannula was assembled with an optical fiber (0.66 NA, 250 µm core) (Prizmatix) secured into a zirconia ferrule (1.25 mm O.D.) (Prizmatix) with non-fluorescent epoxy (Thorlabs). To determine the intensity of light exiting fibers, the output of fibers was measured with a power meter (Thorlabs). Cannulae were fixed to the skull using dental cement (Parkell).

Behavioral testing

135 *In vivo* optogenetic interrogation was performed 1–2 weeks after fiber implantations. Behavioral tests were performed between 2:00 pm and 7:00 pm. *In vivo* optogenetic experiments were performed in an opaque white plastic open-field box (28 cm × 28 cm), which was cleaned with 70% ethanol. On the day prior to optogenetic experiments, each mouse was allowed to acclimate to the open-field box for twenty minutes, with a fiber optic cable attached to the implant via a rotary joint (Prizmatix). Pre-trial, basal ambulatory activity was collected for five 140 minutes at the beginning of the behavioral session. For ChR2 activation, mice were subjected to either a single, sustained light pulse or a patterned pulse train (5 ms pulses at 20 Hz) delivered for 10 s. For GtACR2 activation, only the sustained protocol was used. A blue (peak, ~455 nm) LED (Prizmatix) was used to activate both opsins. The light power used for opsin activation was 12–18 mW measured at the fiber tip. Stimuli were delivered with a one-minute intertrial interval. An overhead camera (Logitech) was used to acquire mouse behavior in the open 145 field arena at 30 fps, 640 pixels × 240 pixels per frame. Videos were subsequently cropped and downsampled to 10 fps at full resolution for markerless tracking.

Behavioral tracking and classification

DeepLabCut (https://github.com/DeepLabCut/) (Mathis et al., 2018; Nath et al., 2019) was used for tracking body 150 parts of mice in an open field arena. Eight body parts including the nose, ears, body center, side laterals (hip-joints), tail base, and tail end were labeled in top-down view videos (**Figure 6c**). To create the training dataset, 1,674 distinct frames from 50 video recordings of open field behavior were manually annotated. We used MobileNetV2-1-based network (Sandler et al., 2018; Mathis et al., 2019) with default parameters. The network was trained and refined for five rounds using default multi-step learning rates. Each round consists of 240,000–1,000,000 155 iterations, and the default multi-step learning rates were used. This trained network has a test error of 1.13 pixels and a training error of 4.82 pixels. Predictions of X-Y coordinates were processed using a median filter with a rolling window of five frames before further analysis. To cross-validate our network performance, speeds computed from DeepLabCut and Ethovision data were compared; near-identical results were obtained (see Results). This network was then used to analyze all videos in this study.

160 To categorize motor behavior, DeepLabCut tracking data were first calibrated; the pixel-to-cm conversion

for each video was determined by comparing the width of the arena in pixels to the actual width of the arena (28 cm). Based on the calibrated X-Y coordinates of labeled body parts, a set of movement metrics was generated for each frame. Mouse speed was measured as the body center speed. Body angle was defined as tail base–nose angle relative to the body center. An angle < 180° indicates the body axis is skewed to the right, and an angle > 180° indicates the body axis is skewed to the left. Mouse width was measured as the euclidean distance between the side laterals and mouse length was measured as the euclidean distance between the nose and the tail base. Locomotion was defined as frames when the body center had a speed > 0.5 cm/s; motionless was defined as frames when ears, the body center, laterals, and the tail base all had a speed ≤ 0.5 cm/s. To classify rearing, we constructed a random forest classifier in SimBA. 19,058 rearing frames from 35 video recordings of open field behavior were extracted and manually annotated as rearing by three independent annotators. Supported and unsupported rearing behaviors were not differentiated. The start frame was defined as the frame in which the mouse lifted its forelimbs off the floor and extended its head upwards; the end frame was defined as the frame before the forelimbs made contact with the floor. The model was built with the following settings: n_estimators = 2,500, RF_criterion = entropy, RF_max_features = sqrt, RF_min_sample leaf = 2, and no oversampling or undersampling. 20% of the video frames were used for testing and the other 80% were used for training. The resulting classifier has a F1-score = 0.71, precision = 0.68, and recall = 0.74. The performance of this classifier was on par with those reported recently (Nilsson et al., 2020). The discrimination threshold was set at Pr = 0.31, and each instance of rearing has a minimum duration of 300 ms. Lastly, fine movements were defined as frames that do not fall into any of the categories mentioned above (i.e., locomotion, motionless, or rearing). Finally, example videos and the trained model are available on Github (https://github.com/saviochan/SimBA-OpenFieldArena) and Zenodo (https://zenodo.org/record/3964701#.XyB8yJ5KhPZ). The data generated by the analysis pipeline were processed using custom Python Scripts. Codes are available online (https://github.com/saviochan/Python-Scripts/tree/master/OpenFieldArena_Behavior). Twenty-five different movement metrics were tracked. Event frequency, duration, and percent time spent were logged. Fold changes were calculated by dividing the movement metric during light-period by that in pre-period. 'Light-period' corresponds to 10 s of light delivery. 'Pre-period' and 'post-period' correspond to the 10-second epoch before and after light delivery, respectively.

To assess the relationship between the measured movement metrics, a correlation matrix was constructed from binned, time-series data. Rearing-motionless switch frequency and motionless-rearing switch frequency were excluded because of the low occurrence of events. Hierarchical clustering of movement metrics
190 was performed in ClustVis (https://biit.cs.ut.ee/clustvis/) (Metsalu and Vilo, 2015). Twenty-five movement metrics were included in the analysis. Mice with targeted optogenetic stimulation of Foxp2$^+$ neurons, Kcng4$^+$ neurons, Npas1$^+$ neurons, and PV$^+$ neurons, were included. Both rows and columns were clustered using correlation distance and average linkage. Movement metrics were centered and scaled. A *K*-nearest neighbors classification algorithm was implemented in JASP to construct a decision boundary matrix. All variables were scaled to have a
195 mean of 0 and a standard deviation of 1. The data were split as follows: 60% training, 20% testing, and 20% validation.

Visualized *ex vivo* electrophysiology

Mice in the age range postnatal day 55–100 were anesthetized with a ketamine-xylazine mixture and perfused
200 transcardially with ice-cold aCSF containing the following (in mM): 125 NaCl, 2.5 KCl, 1.25 NaH_2PO_4, 2.0 $CaCl_2$, 1.0 $MgCl_2$, 25 $NaHCO_3$, and 12.5 glucose, bubbled continuously with carbogen (95% O_2 and 5% CO_2). The brains were rapidly removed, glued to the stage of a vibrating microtome (Leica Instrument), and immersed in ice-cold aCSF. Parasagittal slices containing the GPe were cut at a thickness of 240 μm and transferred to a holding chamber where they were submerged in aCSF at 37 ºC for 30 min and returned to room temperature for recording. Slices
205 were then transferred to a small-volume (~0.5 ml) Delrin recording chamber that was mounted on a fixed-stage, upright microscope (Olympus). Neurons were visualized using differential interference contrast optics (Olympus), illuminated at 735 nm (Thorlabs), and imaged with a 60× water-immersion objective (Olympus) and a CCD camera (QImaging). Genetically-defined neurons were identified by somatic eGFP or tdTomato fluorescence examined under epifluorescence microscopy with a daylight (6,500 K) LED (Thorlabs) and appropriate filters (Semrock).

210 Recordings were made at room temperature (20–22 ºC) with patch electrodes fabricated from capillary glass (Sutter Instrument) pulled on a Flaming-Brown puller (Sutter Instrument) and fire-polished with a microforge (Narishige) immediately before use. Pipette resistance was typically ~3–5 MΩ. For cell-attached and current-clamp recordings, the internal solution consisted of the following (in mM): 135 $KMeSO_4$, 10 Na_2phosphocreatine, 5 KCl, 5

EGTA, 5 HEPES, 2 Mg_2ATP, 0.5 $CaCl_2$, and 0.5 Na_3GTP, with pH adjusted to 7.25–7.30 with KOH. For voltage-clamp
215 recordings of inhibitory postsynaptic currents (IPSCs), a high-chloride internal solution consisted of the following (in mM): 120 CsCl, 10 Na_2phosphocreatine, 5 HEPES, 5 tetraethylammonium-Cl, 2 Mg_2ATP, 1 QX314-Cl, 0.5 Na_3GTP, 0.5 $CaCl_2$, 0.25 EGTA, and 0.2% (wt/vol) biocytin, pH adjusted to 7.25–7.30 with CsOH and a low-chloride internal solution consisted of the following (in mM): 125 $CsMeSO_3$, 10 Na_2-phosphocreatine, 5 tetraethylammonium chloride, 5 QX-314 Cl, 5 HEPES-K, 5 EGTA-K, 2 Mg_2ATP, 0.5 $CaCl_2$, 0.5 Na_3GTP, 0.2% (w/v)
220 biocytin, with pH adjusted to 7.25–7.30 with CsOH. Stimulus generation and data acquisition were performed using an amplifier (Molecular Devices), a digitizer (Molecular Devices), and pClamp (Molecular Devices). For current-clamp recordings, the amplifier bridge circuit was adjusted to compensate for electrode resistance and was subsequently monitored. The signals were filtered at 1 kHz and digitized at 10 kHz. $KMeSO_4$ and Na_2-GTP were from ICN Biomedicals and Roche, respectively. All other reagents were obtained from Sigma-Aldrich.

225 For optogenetic experiments, blue excitation wavelength (peak, ~450 nm) from two daylight (6,500 K) LEDs (Thorlabs) was delivered to the tissue slice from both a 60× water immersion objective and a 0.9 numerical aperture air condenser with the aid of 520 nm dichroic beamsplitters (Semrock). Light delivery was made at the site of electrophysiological recordings with a field of illumination of 500–700 μm in diameter. Paired-pulse optogenetic activation of terminals was at 20 Hz with a light duration of 2 ms. To extract the properties of
230 spontaneous IPSCs in identified GPe neurons, an analysis similar to that described in (Higgs and Wilson, 2016) was used. Briefly, an autocorrelation of spontaneous IPSC times was computed, and for each periodic component detected, the periodic peaks were fitted with a model curve to estimate the presynaptic firing frequency, the coefficient of variation (CV) of presynaptic interspike intervals, and the synaptic success probability. The unitary IPSC amplitudes and waveforms were estimated by subdividing spontaneous IPSCs based on their timing with
235 respect to the surrounding periodic input.

The electrophysiological data used in this study were expanded from a previously published dataset (Abecassis et al., 2020). Hierarchical clustering of electrophysiological attributes was performed in ClustVis (https://biit.cs.ut.ee/clustvis/) (Metsalu and Vilo, 2015). All cell-attached and whole-cell measurements were included in this analysis. Both rows and columns were clustered using correlation distance and average linkage.
240 Electrophysiological measurements were centered and scaled. Principal component analysis of

electrophysiological attributes was performed using the R programming language. t-SNE (k = 2) was performed in JASP using the Hartigan-Wong algorithm with the exact same dataset that was used for hierarchical clustering. All variables were scaled. Partial correlation networks based on Pearson coefficients of electrophysiological parameters were analyzed in JASP and Cytoscape (Shannon et al., 2003) with the CentiScaPe plug-in (Scardoni et al., 2009). The complete dataset for electrophysiological measurements of the intrinsic properties and an interactive web tool can be found online: https://graceyichen.shinyapps.io/neuro_interactive_analysis/.

Drugs

R-CPP and NBQX disodium salt were obtained from Tocris. CGP55845 and QX314-Cl were obtained from Abcam. Na_3GTP and tetrodotoxin were from Roche and Alomone Laboratories, respectively. Other reagents not listed above were from Sigma-Aldrich. Drugs were dissolved as stock solutions in either water or DMSO and aliquoted and frozen at –30 ºC prior to use. Each drug was diluted to the appropriate concentrations by adding to the perfusate immediately before the experiment. The final concentration of DMSO in the perfusate was < 0.1%.

Experimental design and statistical analyses

General graphing and statistical analyses were performed with MATLAB (MathWorks), Prism (GraphPad), JASP (https://jasp-stats.org) and the R programming language (https://www.r-project.org). Custom analysis codes are available on GitHub (https://github.com/chanlab). Sample size (n value) is defined by the number of observations (i.e., neurons, sections, or mice). When percentages are presented, *n* values represent only positive observations. No statistical method was used to predetermine sample size. Data in the main text are presented as median values ± median absolute deviations (MADs) (Leys et al., 2013) as measures of central tendency and statistical dispersion, respectively. Box plots are used for graphic representation of population data unless stated otherwise (Krzywinski and Altman, 2014; Streit and Gehlenborg, 2014; Nuzzo, 2016). The central line represents the median, the box edges represent the interquartile ranges, and the whiskers represent 10–90th percentiles. Normal distributions of data were not assumed. Individual data points were visualized for small sizes or to emphasize variability in the datasets. Non-parametric statistics were used throughout. Comparisons of unrelated samples were performed using a Mann–Whitney U test and comparisons of paired samples were performed using the Wilcoxon signed

rank test. The Kruskal-Wallis test was used to compare multiple groups, followed by the *post hoc* Dunn test to assess pairwise differences while adjusting for the number of pairwise comparisons. The Spearman exact test was used for evaluating correlation between variables with a threshold (α) of 0.05 for significance. Unless < 0.0001 or > 0.99, exact P values (two-tailed) are reported in the text. To avoid arbitrary cutoffs and visual clutter, levels of significance are not included in the figures. Statistical significance is assessed at a significance level of 0.05, after applying the Bonferroni correction to adjust for the number of comparisons.

Results (3816 words)

Recent single-cell transcriptomic analyses have revealed four distinct neuron clusters (Saunders et al., 2018) within the GPe. In addition to the well-established Npas1$^+$-Foxp2$^+$ neurons (blue) that form a subclass of Npas1$^+$ neurons, Npas1$^+$-Nkx2.1$^+$ neurons (cyan) are the other subclass of Npas1$^+$ neurons (**Figure 1a**). Furthermore, PV$^+$ neurons can be subdivided into two clusters (red and teal) with differential expression of Npr3, Kcng4, and Npy2r. Raw data showing the expression patterns of Npr3, Kcng4, and Npy2r can be found online (http://dropviz.org/?_state_id_=6c13807c8420bc74). The expression of these markers in adult GPe is in agreement with results from *in situ* hybridization (**Figure 1b**). While sparse signals were found with Npr3 and Kcng4, the signals associated with Npy2r were widespread through the GPe. Here, we sought to examine whether Npr3-Cre (Daigle et al., 2018), Kcng4-Cre (Duan et al., 2014), and Npy2r-Cre (Chang et al., 2015) mice could provide genetic access to unique GPe subpopulations.

Novel driver lines capture distinct neuron populations

To study Npr3$^+$ neurons, tdTomato-expressing (tdTomato$^+$) neurons in Npr3-L-tdTomato mice were used. Npr3$^+$ neurons were 14% of GPe neurons (14 ± 1%, *n* = 3 sections, 270 neurons). ~90% of Npr3$^+$ neurons were Npas1$^+$ (89 ± 4%, *n* = 4 sections, 474 neurons), 74% were Nkx2.1$^+$ (74 ± 0%, *n* = 3 sections, 169 neurons), 2% were Foxp2$^+$ (2 out of 170 neurons) (**Figure 1d**). To visualize the axonal projection pattern of Npr3$^+$ neurons, ChR2-eYFP was transduced. This resulted in clear axonal arborization within the GPe, in addition to strong eYFP signals in the thalamic reticular nucleus, cortex, and substantia nigra pars compacta (**Figure 1c**). Our data are in line with the

295 recent report that Lhx6$^+$ GPe neurons strongly target compacta neurons (Evans et al., 2019). In summary, Npr3$^+$ neurons had molecular and projectional properties that were completely consistent with those of Npas1$^+$-Nkx2.1$^+$ neurons (Abecassis et al., 2020). These findings further the idea that Npas1$^+$-Nkx2.1$^+$ neurons, along with the previously identified Npas1$^+$-Foxp2$^+$ neurons, are unique GPe neuron types and corroborate the findings in our recent study (Abecassis et al., 2020).

300 In addition to the robust expression in the thalamic reticular nucleus, *in situ* hybridization suggested that Kcng4 is expressed in a subset of neurons in the GPe. To further examine the molecular properties of Kcng4$^+$ neurons, we performed immunohistological studies utilizing the Kcng4-L-tdTom genetic cross. As shown in **Figure 1c**, the majority of Kcng4$^+$ neurons (tdTomato$^+$) express PV (90 ± 10%, *n* = 3 sections, 121 neurons) and they represent ~30% (28 ± 8%, *n* = 3 sections, 121 neurons) of the PV$^+$ population and 10% (10 ± 6%, *n* = 3 sections, 131

305 neurons) of the entirety of the GPe. These data are consistent with the single-cell transcriptomic data (Saunders et al., 2018) and show that Kcng4$^+$ neurons are a subtype of PV$^+$ neurons in the GPe. Using a Cre-inducible synaptophysin-GFP virus, we uncovered that Kcng4$^+$ neurons send axonal projections to subthalamic nucleus (STN), internal globus pallidus, and substantia nigra pars reticulata. No additional projection targets were observed (**Figure 1c**).

310 To label Npy2r$^+$ neurons, a similar genetic strategy was used. tdTomato$^+$ neurons from Npy2r-L-tdTomato mice were studied. As expected from the single-cell transcriptomic and *in situ* hybridization data, a large fraction (~70%) of GPe neurons were tdTomato$^+$. In addition to a labeled population of GPe neurons, striosomes throughout the striatum were labeled in the Npy2r-L-tdTom cross and appeared to be largely devoid of cell body labeling. The tdTomato$^+$ neurons in the striatum were likely interneurons, based on their density (**Figure 2a**).

315 Though single-cell transcriptomic data suggest a broad expression profile of Npy2r among GPe neurons, whether the Npy2r-Cre mouse line would provide genetic access to selective neuron subtypes has not been tested. To this end, we transduced ChR2-eYFP to Cre$^+$ neurons in Npy2r-Cre mice. This yielded axonal labeling patterns that were the most consistent with Npr3$^+$ (aka Npas1$^+$-Nkx2.1$^+$) neurons (c.f. **Figure 1c**). In contrast, only sparse or weak axonal labeling was observed in canonical targets of PV$^+$ neurons, i.e., STN and SNr (**Figure 2b**). The unexpected

320 results prompted us to further examine the unusual properties of the Npy2r-Cre line. As roughly half of the tdTomato$^+$ neurons (53 ± 8%, *n* = 11 sections, 1319 neurons) from Npy2r-L-tdTomato mice were PV$^+$ (not shown),

we decided to selectively study PV$^+$-Npy2r$^+$ neurons using the PV-Npy2r-FL-tdTom genetic cross (**Figure 2c**). PV$^+$-Npy2r$^+$ neurons accounted for ~65% (63 ± 4%, *n* = 11 sections, 1319 neurons) of the PV$^+$ population and amounted to ~35% (34 ± 1%, *n* = 3 sections, 392 neurons) of the entire GPe. The somatodendritic morphology of PV$^+$-Npy2r$^+$ neurons examined were also consistent with that of PV$^+$ neurons (**Figure 2d**). To our surprise, a genetic PV-Npy2r-FL-tdTom cross yielded tdTomato expression not only in PV$^+$ neurons but also in a very small fraction of PV$^-$ neurons (**Figure 2c**). One caveat of the FSF-LSL-tdTomato reporter strains is that they allow for very effective recombination, even for strains that have weak Cre activity. However, in strains that have high Cre activity, atypical expression patterns can be observed (Madisen et al., 2010).

GPe neurons cluster into two electrophysiological groups

To study the electrophysiological properties of Npr3$^+$ neurons, Kcng4$^+$ neurons, Npy2r$^+$ neurons, and PV$^+$-Npy2r$^+$ neurons, we performed *ex vivo* patch-clamp recordings using near-identical procedures described previously. To make sense of the results, we combined these data with an expanded version of a previously published dataset (Abecassis et al., 2020). Univariate scatter plots were used to emphasize the variability across samples. Corroborating the histological data, electrophysiological analysis showed that Npr3$^+$ neurons and Kcng4$^+$ neurons are a subset of the Npas1$^+$ class and PV$^+$ class, respectively. It is notable that Npr3$^+$ neurons display properties that are indistinguishable from Npas1$^+$-Lhx6$^+$ neurons and Lhx6$^+_{bright}$ neurons. Apart from a strong tendency of Foxp2$^+$ neurons and PV$^+$ neurons to be on opposite ends of the spectrum, data are largely graded (**Figure 3**). Given that Kcng4 is an ion channel gene, it is surprising that the expression of Kcng4 did not confer unique electrophysiological properties.

To more effectively visualize how Npr3$^+$ neurons, Kcng4$^+$ neurons, Npy2r$^+$ neurons, and PV$^+$-Npy2r$^+$ neurons co-cluster with other known GPe neuron types, we performed principal component analysis (PCA) and a variety of clustering approaches on the previously published datasets (Abecassis et al., 2020) along with our newly collected dataset, which includes PV$^+$-Lhx6$^+$ neurons and Npas1$^+$-Lhx6$^+$ neurons. Hierarchical clustering yielded two clusters that are largely consistent with the PV$^+$ class and Npas1$^+$ class. As there was no *a priori* information on whether PV$^+$ neurons can be subdivided based on their electrophysiological attributes, we clustered all identified PV$^+$ neurons (*n* = 100) separate from the rest of the dataset (**Figure 4a**). t-SNE plots were used for visualizing high-

dimensional data in a low-dimensional space. The relative distances between each marker represent similarities in the electrophysiological attributes. This analysis agreed with the PCA, in that two main clusters can be identified (**Figure 4b**). The PCA analysis shows that 45% of the total variance is explained by the first component and only 16% by the second component. The PCA biplot also shows the relative variance of each variable and their contribution to each principal component (**Figure 4c**). Maximal firing rate, maximal current, spike width, and trough potential made the most contributions to the first principal component. In contrast, the first action potential height and membrane potential contributed the least.

To better understand the relationship between individual attributes, we performed network analysis with the dataset. Subtle differences between the PV^+ neuron and $Npas1^+$ neuron networks were found (**Figure 4d**). A correlation between maximal firing rate, maximal current, and action potential width is consistent between the two networks and is conceivable as a function of congruent expression of voltage-gated sodium and potassium channels in these neurons (Hernandez et al., 2015).

Markerless tracking effectively extracts behavioral dynamics

To investigate the roles of specific GPe populations in motor control, we analyzed the behavior of freely moving mice in an open field. As the basal ganglia are known to control complex body kinematics (Turner and Anderson, 1997; Turner et al., 1998; Desmurget and Turner, 2010; Jin et al., 2014; Rueda-Orozco and Robbe, 2015; Klaus et al., 2017; Markowitz et al., 2018; Park et al., 2020), we tracked body kinematics using machine learning approaches. To accomplish this, we established a DeepLabCut (Mathis et al., 2018; Nath et al., 2019) model to track the two-dimensional coordinates of eight body parts (**Figure 5a**). The model was trained until the loss reached a plateau. This trained network had a test error of 1.13 pixels and a training error of 4.82 pixels. This error was negligible relative to the mouse size—the median mouse width and length were 65.2 ± 4.5 pixels and 152.8 ± 20.0 pixels, respectively. Speeds computed from the tracking data generated from DeepLabCut and Ethovision were tightly correlated, confirming the validity of our model (**Figure 5c**).

To understand the motor patterns of mice in an open field, we defined locomotion, fine movement, and motionless based on the movements of body parts (**Figure 5a**). To describe the full repertoire of motor behavior, we captured rearing behavior by building a random forest classifier in SimBA (Nilsson et al., 2020). This classifier

has a F1-score = 0.71, precision = 0.68, and recall = 0.74 (**Figure 5c**). Using this machine learning pipeline, we were able to effectively quantify behavioral events of mice in the open field in much greater detail and detect more complex, yet subtle, changes in body kinematics than before (**supplemental video**). We quantified the four different behaviors in PV-Cre and Npas1-Cre mice (*n* = 28 mice). At the population level, time spent in each category was: 55.8% in locomotion, 25.2% in fine movement, 10.0% in rearing, and 8.4% in motionless (**Figure 5b**).

Our previous studies established that PV^+ neurons and $Npas1^+$ neurons play causal, but opposite roles in regulating locomotion—PV^+ neurons are movement-promoting and $Npas1^+$ neurons are movement-suppressing (Glajch et al., 2016; Pamukcu et al., 2020). Consistent with our earlier observations, our analysis here showed that mice exhibited more mobile behavior (i.e., locomotion) when PV^+ neurons were optogenetically stimulated and more immobile behavior (i.e., fine movement and motionless) when $Npas1^+$ neurons were optogenetically stimulated. On the other hand, rearing was not consistently altered by optogenetic perturbations of either PV^+ neurons or $Npas1^+$ neurons (**Figure 5d**). This provides a proof-of-concept that the network can be used effectively to extract body kinematics in mice. To monitor the orientation and posture of the mice, we measured the body angle and length-width ratio, respectively (**Figure 5e**). A correlation matrix was constructed to visualize the relationships between different movement metrics (**Figure 5f**). Spearman rank correlation tests between pairs of variables showed that 10 of the 21 pairs were correlated after the Bonferroni correction: locomotion was correlated with fine movement, rearing, body ratio, and speed; fine movement was correlated with motionless, body ratio, and speed; motionless was correlated with body ratio and speed; and body ratio was correlated with speed. In particular, the average event counts of fine movement and motionless were positively correlated with each other. Locomotion was associated with a high length-width ratio and a high speed, indicating that the mouse assumed an elongated form during locomotion. fine movement and motionless were associated with a low length-width ratio and a low speed, which is indicative of a hunched and retracted posture. Similarly, body angle correlated with moment-to-moment changes in speed and body ratio (**Figure 5e**).

Optogenetic manipulations induce cell-specific motor patterns

As a large number of parameters (a total of 25) including movement sequences were tracked, we examined the relationships between the measured parameters by constructing a correlation matrix for both PV-Cre and Npas1-

Cre mice that were used in this study (*n* = 28). We found strong correlations between a large number of variable-pairs (163 from 253), assessed via Spearman rank correlation tests after the Bonferroni correction. As mice have low incidences of transitioning between rearing and motionless, rearing-motionless and motionless-rearing switch frequencies were excluded from this analysis. At this point, it is unclear if that was hardwired in the motor program or if it was constrained by body mechanics. Data from pre- and light-periods were combined, as no marked differences in the relationships between movement metrics were noted (not shown). A condensed version of the correlation matrix that contains the most relevant metrics are presented in **Figure 6a**. For example, percent time spent on locomotion positively correlated (blue) with speed but negatively correlated (brown) with percent time spent on fine movement and motionless. To effectively visualize the motor behaviors in mice when PV$^+$ neurons and Npas1$^+$ neurons were optogenetically stimulated, we performed a PCA. As shown in **Figure 6a,** mice showed very similar behavior during the pre-period. In contrast, they showed divergent responses when PV$^+$ neurons and Npas1$^+$ neurons were optogenetically stimulated during the light-period.

Figure 6b is a heatmap representation of a hierarchical clustering analysis of movement metrics showing coordinated changes in behavioral dynamics upon the stimulation of genetically-defined GPe neurons. Foxp2$^+$ neurons, Kcng4$^+$ neurons, Npas1$^+$ neurons, and PV$^+$ neurons transduced with ChR2-eYFP were included in this analysis. Unlike the ethograms in **Figure 5d** that are purely event-counting across time, the heatmap in **Figure 6b** shows the fold changes of all 25 movement metrics in response to optogenetic stimulation. The most striking effects were the changes in speed, locomotion duration, percent time in motionless, and motionless frequency. The raw data for speed is shown in **Figure 6c**. To contextualize the magnitude of the observed effect, direct- and indirect-pathway striatal projection neurons (dSPNs and iSPNs, respectively) were included for comparison. **Figure 6d** shows the changes in total, locomotion, fine movement, and motionless frequencies across individual mice. The subtle differences between mouse lines made it difficult to make arguments about quantitative differences. With this caveat in mind, it is nevertheless surprising to see that optogenetic stimulation of Kcng4$^+$ neurons produced statistically indistinguishable effects on locomotor speed as PV$^+$ neurons. This result was not expected as Kcng4$^+$ neurons only account for ~10% of the entirety of the GPe. Similarly, optogenetic stimulation of Foxp2$^+$ neurons produced near-identical effects on locomotor speed as Npas1$^+$ neurons (**Table 3**), while they only account for ~25% of the entirety of the GPe (**Figure 1d**).

430 Given Kcng4$^+$ neurons are ~30% (28 ± 8%, *n* = 3 sections, 121 neurons) of PV$^+$ neurons and Foxp2$^+$ neurons are ~60% (57 ± 4%, *n* = 6 sections, 566 neurons) of Npas1$^+$ neurons, our results raised a question of whether PV$^+$-Kcng4$^-$ neurons and Npas1$^+$-Foxp2$^-$ neurons could be involved in non-motor function. Close examination of the movement tracks revealed that optogenetic stimulation of PV$^+$ neurons and Npas1$^+$ neurons led to changes in the anxiety levels, as measured by their center-edge preference in the open-field arena. As shown in **Figure 6e** & **f**, PV$^+$
435 neuron stimulation decreased the time spent at the center, while Npas1$^+$ neuron stimulation increased it (PV$^+$ pre: 47.3 ± 10.3%, PV$^+$ light: 27.4 ± 5.4%, *n* = 12, P = 0.0034; Npas1$^+$ pre: 27.3 ± 10.4%, Npas1$^+$ light: 35.7 ± 12.3%, *n* = 16, P = 0.0060). These effects were highly cell type-specific as they were not observed with the stimulation of Kcng4$^+$ neurons, Foxp2$^+$ neurons, dSPNs, or iSPNs and thus were dissociable from the locomotor effects (Kcng4$^+$ pre: 17.7 ± 7.9%, Kcng4$^+$ light: 16.9 ± 4.1%, *n* = 8, P = 0.38; Foxp2$^+$ pre: 11.5 ± 10.7%, Foxp2$^+$ light: 10.4 ± 8.7%, *n* =
440 18, P = 0.30; dSPN pre: 24.1 ± 19.0%, dSPN light: 13.1 ± 4.1%, *n* = 9, P = 0.10; iSPN pre: 18.6 ± 7.2%, iSPN light: 18.6 ± 9.6%, *n* = 11, P = 0.90).

Combinatorial movement metrics infers behavioral states

To visualize how every observation would be classified, we constructed a decision boundary matrix using a *K*-
445 nearest neighbors classification algorithm (**Figure 7a**). As illustrated by the receiver operating characteristic (ROC) curves in **Figure 7b**, each neuron type studied here gave rise to unique behavior structures. This analysis showed that a number of neuron types occupied a unique parameter space as delineated by the decision boundaries visualized (e.g., **Figure 7c**). As shown in the relationship between locomotion frequency and the percent time in locomotion (**Figure 7c**), PV$^+$ neurons and Npas1$^+$ neurons were on opposite ends of the spectrum. This suggests
450 that PV$^+$ neurons and Npas1$^+$ neurons work against each other. On the other hand, PV$^+$ neurons, Kcng4$^+$ neurons, dSPNs, and STN neurons (transduced with GtACR2, an inhibitory opsin) were close to one another, suggesting that these neurons work either together or converge on a common downstream target to mediate the same action. This idea is supported by experimental evidence that PV$^+$ neurons and Kcng4$^+$ neurons send inhibitory signals to the substantia nigra pars reticulata, which receive direct inhibitory inputs from dSPNs. In contrast, iSPNs that are
455 known to heavily target PV$^+$ neurons (but not PV$^-$ neurons) (Yuan et al., 2017) are on the lower-left corner of the

plot. This analysis reinforced the notion that the differences in the tracked motor behaviors were in fact cell-specific and not simply esoteric fluctuations.

As noted earlier, as PV^+ neurons and $Npas1^+$ neurons produced diametric behavioral effects, we asked whether PV^+ neurons and $Npas1^+$ neurons could be working in concert to regulate the transitions between two behavioral states in mice. Instead of simply providing granularity of behavioral dynamics, we sought to determine if we can use the different movement metrics collectively to define behavioral states. To this end, we parsed out the data from both PV-Cre and Npas1-Cre mice during both pre- and light-periods and then performed a *k*-means clustering (with $k = 2$) that included all 25 movement metrics. In **Figure 7d**, the dimensionality of the data is reduced via t-SNE, with each mouse shaded according to which cluster it is assigned to. As expected, the predicted cluster memberships for cluster 1 and 2 were about evenly split in both PV-Cre and Npas1-Cre mice during the pre-period (PV: 56.3%, Npas1: 41.7%). However, optogenetic stimulation shifted the membership distributions—PV-Cre mice were predominantly (75.0%) in cluster 1, whereas Npas1-Cre were predominantly (81.3%) in cluster 2 during the light-period.

The *k*-means clustering analysis thus provided critical insights. First, it reinforced the idea that optogenetic manipulations of PV^+ neurons and $Npas1^+$ neurons gave rise to physiological behaviors. Second, the analysis suggests that the combinations of movement metrics can be used to define two behavioral states and supports the notion that PV^+ neurons and $Npas1^+$ neurons act as opposing forces that tune mouse behavior.

Local collateral connectivity within the GPe is cell-specific

Here, we hypothesized that PV^+ neurons and $Npas1^+$ neurons communicate via inhibitory connections. Consistent with prior observations from single-cell labeling studies (Kita and Kitai, 1994; Nambu and Llinas, 1997; Bevan et al., 1998; Sato et al., 2000; Sadek et al., 2007; Fujiyama et al., 2016), biocytin-filled GPe neurons produced local collaterals that contain large varicosities that can be readily observed *post hoc* with confocal microscopy (**Figure 8a**). Though, with this approach, the postsynaptic partner cannot be easily identified.

The presence of local inhibitory networks was further supported by the presence of large, periodic inhibitory postsynaptic currents in voltage-clamp recordings with a high-chloride internal solution. As expected from the

pallidal origin, these events are action potential-dependent, as demonstrated by their sensitivity to the application of tetrodotoxin (1 μM), a voltage-gated sodium channel blocker (**Figure 8b**).

To gain further insights into the local connectivity, spontaneous IPSCs were recorded from PV^+ neurons and $Npas1^+$ neurons; properties of periodic and aperiodic IPSCs were extracted using our established analysis routine (Higgs and Wilson, 2016) (**Figure 8c**). In agreement with the results in **Figure 8b**, the small amplitude aperiodic events were likely of striatal origin, whereas the large amplitude periodic events arose from local collateral inputs. Furthermore, this analysis revealed that PV^+ neurons and $Npas1^+$ neurons receive local inputs and display IPSCs with very similar biophysical properties (**Table 4**).

While it is probable that PV^+ neurons and $Npas1^+$ neurons are reciprocally connected to each other via inhibitory connections, the precise local connectivity patterns between GPe neurons have not been examined previously. As termination sites produced by local axonal arborizations are sparse and spatially distributed within the GPe (Kita and Kitai, 1994; Nambu and Llinas, 1997; Bevan et al., 1998; Sato et al., 2000; Sadek et al., 2007; Bugaysen et al., 2013; Fujiyama et al., 2016), an optogenetic approach instead of paired recordings was used to more efficiently survey the local connectivity patterns. ChR2-eYFP was transduced into genetically-defined neurons in PV-Cre and Npas1-Cre mice, using a Cre-inducible approach. Transgene negative neurons were targeted for voltage-clamp recordings. As illustrated in **Figure 8d**, optogenetic stimulation of PV^+ neurons induced antiphase timing of a spontaneous synaptic input, suggesting antiphase spiking of a putative PV^- neuron. This is more clearly shown in the peristimulus time histogram in **Figure 8e**. These results highlight the potential of local collateral input to shape population activity across the GPe. Using similar approaches, we tested the connectivity of PV^+ to PV^-, $Npas1^+$ to $Npas1^-$, and $Foxp2^+$ to PV^+ (**Figure 8f** & **g**). To avoid confounds associated with photocurrents, ChR2-eYFP negative neurons were targeted for recording. We found that PV^+ to PV^- input was the strongest of all connection types examined (PV^+ to PV^-: 409.9 ± 233.0 pA, n = 19 neurons; $Npas1^+$ to $Npas1^-$: 75.1 ± 59.2 pA, n = 15 neurons; $Npas1^+$ to PV^+: 62.2 ± 44.0 pA, n = 39 neurons; $Foxp2^+$ to PV^+: 13.3 ± 2.0 pA, n = 8 neurons; PV^+ to PV^- vs. $Npas1^+$ to $Npas1^-$, $P = 0.0024$; PV^+ to PV^- vs. $Npas1^+$ to PV^+, $P < 0.0001$; PV^+ to PV^- vs. $Foxp2^+$ to PV^+, $P = 0.00023$; $Npas1^+$ to $Npas1^-$ vs. $Npas1^+$ to PV^+, $P = 0.53$; $Npas1^+$ to $Npas1^-$ vs. $Foxp2^+$ to PV^+, $P = 0.0053$; $Npas1^+$ to PV^+ vs. $Foxp2^+$ to PV^+, $P = 0.0047$). This finding is consistent with the earlier observation that PV^+ boutons are abundant and form basket-like aggregates on cell bodies of both PV^+ and PV^- neurons within the GPe

(Kita, 1994). Though Npas1$^+$ neurons did target PV$^+$ (which are Npas1$^-$) neurons, the strength was smaller than that of the PV$^+$ to PV$^-$ connection. The asymmetry in the connectivity between PV$^+$ neurons and Npas1$^+$ neurons can be partially explained by their abundance.

Only a subset of recorded PV$^+$ neurons (8 out of 18, 44.4%) showed detectable Foxp2$^+$ input, and the strength of this connection was the weakest among all connection types examined (Foxp2$^+$ to PV$^+$ vs. PV$^+$ to PV$^-$, P = 0.00023; Foxp2$^+$ to PV$^+$ vs. Npas1$^+$ to Npas1$^-$, P = 0.0053; Foxp2$^+$ to PV$^+$ vs. Npas1$^+$ to PV$^+$, P = 0.0047). The observation of this weak and likely biologically negligible connection is highly consistent with recent studies (Aristieta et al., 2020; Ketzef and Silberberg, 2020). As it was clear that the Npas1$^+$ input targets PV$^+$ neurons, these results collectively imply that PV$^+$ neurons receive Npas1$^+$ input exclusively from the Nkx2.1$^+$ (aka Npr3$^+$) neurons, which do not express Foxp2 (**Figure 1c**), see also (Abecassis et al., 2020).

Discussion (1849 words)

In this study, we determined that Npr3$^+$ neurons shared the unique molecular and anatomical signature of Npas1$^+$-Nkx2.1$^+$ neurons. While Kcng4$^+$ neurons have canonical properties as PV$^+$ neurons, they were not involved in regulating anxiety-related behavior (as measured with center-edge preferences). By using machine learning and statistical approaches to delineate the functional properties of GPe neuron subtypes, we proposed that PV$^+$ neurons and Npas1$^+$ neurons work in concert to control the transitions between behavioral states in mice. This idea was further supported by the existence of local connectivity between them.

GPe neuron diversity

What is a cell type and why is it an important question? Both the embryonic origins and the congruent expression of transcription factors govern cell specifications (Hu et al., 2017; Lim et al., 2018; Fishell and Kepecs, 2020). It is well-established that the GPe primarily arises from the medial and lateral ganglionic eminence (MGE and LGE) (Flandin et al., 2010; Nobrega-Pereira et al., 2010; Dodson et al., 2015; Chen et al., 2017). It is clear that Npas1$^+$ neurons are derived from both progenitor pools; Foxp2$^+$ neurons are from the LGE, whereas Npr3$^+$ neurons are

535 from the MGE and maintain the expression of Nkx2.1 (**Figure 1c**). Consistent with the single-cell transcriptomic data (Saunders et al., 2018), our current and past (Abecassis et al., 2020) data showed the molecular complexity of PV^+ neurons. This is in agreement with earlier studies that hinted at multiple MGE progenitors giving rise to two populations of PV^+ neurons (Silberberg et al., 2016). In fact, heterogeneity among PV^+ neurons can be a general feature across brain areas (Dehorter et al., 2015; Garas et al., 2016; Tasic et al., 2018; Hodge et al., 2019; Huang
540 and Paul, 2019; Mahadevan et al., 2020). It has been shown that there is sonic hedgehog (Shh) expression in the preoptic area and in the nascent GPe (Flandin et al., 2010; Sousa and Fishell, 2010). In agreement with this, earlier studies on $Dbx1^+$ neurons showed that preoptic area neurons make a small contribution to the cellular makeup of the GPe (Gelman et al., 2011; Abecassis et al., 2020). This inference was confirmed with our recent, progenitor-specific fate-map study (Poulin et al., 2020).

545 Although cellular diversity in the GPe has been recognized since the 70's (DeLong, 1971; Fox et al., 1974), how heterogeneity maps onto molecular and functional differences has been unclear. Our interest was never to understand cell-type *per se*. Instead, by studying cellular composition and the nature of neuronal identity, we hope to uncover molecular markers and genetic tools that allow us to interrogate the organization principles and functions of GPe neuron subtypes. The cellular composition in the GPe is relatively simple, compared to that of
550 the cortex and hippocampus (Jiang et al., 2015; Tasic et al., 2016; Tasic et al., 2018; Huang and Paul, 2019; Yao et al., 2020) the advent of single-cell transcriptomic and mouse genetics has created an opportunity to interrogate the GPe with previously unexplored tools and has enabled us to provide new insights into GPe neuron diversity and its behavioral relevance in this study. A large set of transcription factors have been previously identified to govern the formation of the GPe. We took a leap of faith in generating Npas1-Cre mice and Npas1 antibodies *de*
555 *novo* to interrogate the GPe. This decision was based on the compelling data from prior literature (Flandin et al., 2010; Nobrega-Pereira et al., 2010). While PV-Cre and Npas1-Cre mice will continue to be instrumental to our research, we have now identified a set of transgenic lines that will allow the field to work together to solve more challenging questions and to reconcile discrepancies that arose from suboptimal tools.

Depending upon the metric employed, the definition of cell types differs. This is our first attempt to examine
560 the cellular, circuit, and behavioral properties of $Foxp2^+$ neurons, $Npr3^+$ neurons, $Kcng4^+$ neurons, and $Npy2r^+$ neurons. This study is among the first to show that GPe neuron subclasses have specialized connections and

functions. However, we do not know the relationship between these neuron subtypes and the somatotopic organization of the circuit (Romanelli et al., 2005; Nambu, 2011; Bertino et al., 2020). *In vivo* optogenetics does not offer the resolution to answer this type of question. Our understanding of these neurons, and ultimately the GPe, will undoubtedly continue to be refined, while we await driver lines that offer genetic access to the PV^+-$Kcng4^-$ population.

Beyond go and no-go?

By tracking body kinematics and movement dynamics, we described how optogenetic manipulations of specific cell types gave rise to unique behavioral structures. With this information, we inferred the behavioral states of mice and functional interactions between individual neuron types. We found that upon $Npas1^+$ neuron stimulation, mice were not completely motionless. Instead, they spent more time executing fine movement, which on its own can be mediated by a complex circuit. As motionless and fine movement often co-occurred within a given time period, we interpret fine movement as a manifestation of action suppression. In turn, the basal ganglia are reset for selecting new actions—in this case, locomotion in an open-field arena.

As PV^+ neurons and dSPNs converge onto the substantia nigra pars reticulata (Grofova, 1975; Araki et al., 1985; Bolam et al., 1993; Mink, 1996; Smith et al., 1998; Connelly et al., 2010), it is conceivable that PV^+ neurons and dSPNs are both involved in motor-promotion. Earlier single-cell tracing studies show that SNr-projecting striatal neurons arborize within the GPe (Kawaguchi et al., 1990; Wu et al., 2000; Levesque and Parent, 2005; Fujiyama et al., 2011); however, the postsynaptic targets remain elusive. Our data suggest that they do not target PV^+ neurons. Though the role of the basal ganglia in movement speed has long been recognized (Kornhuber, 1971; DeLong et al., 1984; Yttri and Dudman, 2016; Fobbs et al., 2020), here we argue that the basal ganglia control more than just go and no-go. As the basal ganglia are known to support a wide repertoire of innate complex behaviors (such as rearing and grooming) (Graybiel, 2008; Redgrave et al., 2010; Ahmari, 2016; Markowitz et al., 2018; Park et al., 2020), we should consider using movement dynamics broadly as metrics to measure basal ganglia function rather than relying solely on speed. Our experiments utilized different mouse strains to target selective neuron types for manipulations, and therefore, it is rather difficult to untangle the *bona fide* cell-specific behavioral effects from nuanced differences in behavior across mouse strains. Future experiments that employ intersectional

approaches will yield more definitive answers.

We have recently shown that PV$^+$ neurons and Npas1$^+$ neurons are positioned differently within the basal ganglia. This inference is further supported by *in vivo* whole-cell analysis (Ketzef and Silberberg, 2020). We did not observe marked differences in the electrophysiological properties between neurons within each class. This implies that input-output transformation among them is similar. It is thus probable that neurons within each class receive inputs with similar physiological properties. In turn, both PV$^+$ neurons and Npas1$^+$ neurons exhibit complex projection patterns. It is now clear that this complexity is in part a result of a mixture of neuron subclasses (this study, Mastro et al., 2014; Abdi et al., 2015; Dodson et al., 2015; Hernandez et al., 2015; Fujiyama et al., 2016; Glajch et al., 2016; Hegeman et al., 2016; Abecassis et al., 2020). The formation of these "circuit modules" by neuron subclasses, in turn, dictates the network effects and thus behavioral outcome. We previously examined the GPe output to the dorsal striatum and the STN (Hernandez et al., 2015; Glajch et al., 2016). Given the diametric behavioral effects produced by these two populations of neurons, it was a logical next step to ask if PV$^+$ neuron and Npas1$^+$ neurons are reciprocally inhibiting each other. In this study, by using a combination of transgenic lines, we have overcome some of the challenges associated with the interrogation of cell type-specific connectivity. Our data showed that PV$^+$ neurons and Npas1$^+$ neurons are connected to each other and thus support the idea that the diametric behavioral phenotype observed when one of these two classes of neurons was perturbed was a result of a push-pull function between PV$^+$ neurons and Npas1$^+$ neurons. We found that Foxp2$^+$ neurons completely avoided PV$^+$ neurons. More importantly, this observation suggests that input from Npas1$^+$ neurons to PV$^+$ neurons are provided by Npr3$^+$ (aka Npas1$^+$-Nkx2.1$^+$) neurons exclusively. This inference is consistent with the high density of local axons produced by Npr3$^+$ neurons, as observed in **Figure 1c**. However, we have yet to uncover the properties of the connections made by Npr3$^+$ neurons. In contrast, synaptic tagging experiments suggested that Kcng4$^+$ neurons did not produce local inputs (**Figure 1c**). It will be important to confirm this anatomical observation with functional studies. With the identification of new genetic tools, we should be in a position to study the synaptic connectivity and its alterations at greater depth.

Recent literature emphasized that PV$^+$ neurons are at the intersection of motor-anxiety circuits (Sztainberg et al., 2011; Hunt et al., 2018; Giovanniello et al., 2020) we do not currently know the downstream targets that mediate the anxiety-related response. As the STN does not mediate this anxiety-related response, other

descending pathways such as the direct projections to the raphe (Pollak Dorocic et al., 2014) or their indirect projection to the habenula via the internal globus pallidus (Smith et al., 1998; Wallace et al., 2017) could be involved. While Npas1$^+$ neurons, in particular Foxp2$^+$ neurons, have extensive axonal arborization in the dorsal striatum (Dodson et al., 2015; Hernandez et al., 2015; Glajch et al., 2016), it is important to emphasize that their downstream impact on the somatic excitability of striatal projection neurons is relatively weak (Glajch et al., 2016). The cellular mechanisms that mediate motor-suppression have yet to be identified. While Foxp2$^+$ neurons have been proposed to send "stop" signals to the striatum (Mallet et al., 2016), it is likely that multiple circuit elements are involved in producing complete behavioral arrest (Schmidt et al., 2013; Jahanshahi et al., 2015; Wessel and Aron, 2017). On the other hand, it is rather straightforward that the inhibitory projection to the STN (and substantial pars reticulata) mediates the motor-promoting effects, and it is consistent with the established relationship between STN activity and movement suppression (Verhulst, 1976; Hamani et al., 2004; Aron and Poldrack, 2006; Aron et al., 2007; Eagle et al., 2008; Schmidt et al., 2013; Schweizer et al., 2014; Fife et al., 2017; Wessel and Aron, 2017). In addition to the established literature demonstrating that the GPe sends inhibitory signals to the input and output nuclei of the basal ganglia (Jessell et al., 1978; Mink, 1996; Smith et al., 1998; Kita, 2007; Hegeman et al., 2016), recent studies highlight the existence of cortico-pallido-cortical loops (Saunders et al., 2015; Schwarz et al., 2015; Ahrlund-Richter et al., 2019; Karube et al., 2019; Abecassis et al., 2020; Anastasiades et al., 2020; Clayton et al., 2020), though the precise circuit entities involved have yet to be defined. The direct feedback from Npr3$^+$ (aka Npas1$^+$-Nkx2.1$^+$) neurons to cortical regions (**Figure 1c**, see also (Abecassis et al., 2020)) argues that the action selection is not simply a top-down command.

References

Abdi A, Mallet N, Mohamed FY, Sharott A, Dodson PD, Nakamura KC, Suri S, Avery SV, Larvin JT, Garas FN, Garas SN, Vinciati F, Morin S, Bezard E, Baufreton J, Magill PJ (2015) Prototypic and arkypallidal neurons in the dopamine-intact external globus pallidus. J Neurosci 35:6667-6688.

Abecassis ZA, Berceau BL, Win PH, Garcia D, Xenias HS, Cui Q, Pamukcu A, Cherian S, Hernandez VM, Chon U, Lim BK, Kim Y, Justice NJ, Awatramani R, Hooks BM, Gerfen CR, Boca SM, Chan CS (2020) Npas1(+)-Nkx2.1(+) Neurons Are an Integral Part of the Cortico-pallido-cortical Loop. J Neurosci 40:743-768.

Ahmari SE (2016) Using mice to model Obsessive Compulsive Disorder: From genes to circuits. Neuroscience 321:121-137.

Ahrlund-Richter S, Xuan Y, van Lunteren JA, Kim H, Ortiz C, Pollak Dorocic I, Meletis K, Carlen M (2019) A whole-brain atlas of monosynaptic input targeting four different cell types in the medial prefrontal cortex of the mouse. Nat Neurosci 22:657-668.

Albin RL, Young AB, Penney JB (1989) The functional anatomy of basal ganglia disorders. Trends Neurosci 12:366-375.

Anastasiades PG, Collins DP, Carter AG (2020) Mediodorsal and ventromedial thalamus engage distinct L1 circuits in the prefrontal cortex. bioRxiv:2020.2001.2008.898817.

Anderson ME, Horak FB (1985) Influence of the globus pallidus on arm movements in monkeys. III. Timing of movement-related information. J Neurophysiol 54:433-448.

Araki M, McGeer PL, McGeer EG (1985) Striatonigral and pallidonigral pathways studied by a combination of retrograde horseradish peroxidase tracing and a pharmacohistochemical method for gamma-aminobutyric acid transaminase. Brain Res 331:17-24.

Aristieta A, Barresi M, Lindi SA, Barriere G, Courtand G, de la Crompe B, Guilhemsang L, Gauthier S, Fioramonti S, Baufreton J, Mallet NP (2020) A disynaptic circuit in the globus pallidus controls locomotion inhibition. bioRxiv:2020.2007.2019.211318.

Aron AR, Poldrack RA (2006) Cortical and subcortical contributions to Stop signal response inhibition: role of the subthalamic nucleus. J Neurosci 26:2424-2433.

Aron AR, Durston S, Eagle DM, Logan GD, Stinear CM, Stuphorn V (2007) Converging evidence for a fronto-basal-ganglia network for inhibitory control of action and cognition. J Neurosci 27:11860-11864.

Bertino S, Basile GA, Bramanti A, Anastasi GP, Quartarone A, Milardi D, Cacciola A (2020) Spatially coherent and topographically organized pathways of the human globus pallidus. Hum Brain Mapp.

Bevan MD, Booth PA, Eaton SA, Bolam JP (1998) Selective innervation of neostriatal interneurons by a subclass of neuron in the globus pallidus of the rat. J Neurosci 18:9438-9452.

Bolam JP, Smith Y, Ingham CA, von Krosigk M, Smith AD (1993) Convergence of synaptic terminals from the striatum and the globus pallidus onto single neurones in the substantia nigra and the entopeduncular nucleus. Prog Brain Res 99:73-88.

Boraud T, Bezard E, Guehl D, Bioulac B, Gross C (1998) Effects of L-DOPA on neuronal activity of the globus pallidus externalis (GPe) and globus pallidus internalis (GPi) in the MPTP-treated monkey. Brain Res 787:157-160.

Bugaysen J, Bar-Gad I, Korngreen A (2013) Continuous modulation of action potential firing by a unitary GABAergic connection in the globus pallidus in vitro. J Neurosci 33:12805-12809.

Chan CS, Peterson JD, Gertler TS, Glajch KE, Quintana RE, Cui Q, Sebel LE, Plotkin JL, Shen W, Heiman M, Heintz N, Greengard P, Surmeier DJ (2012) Strain-specific regulation of striatal phenotype in Drd2-eGFP BAC transgenic mice. J Neurosci 32:9124-9132.

Chan CS, Glajch KE, Gertler TS, Guzman JN, Mercer JN, Lewis AS, Goldberg AB, Tkatch T, Shigemoto R, Fleming SM, Chetkovich DM, Osten P, Kita H, Surmeier DJ (2011) HCN channelopathy in external globus pallidus neurons in models of Parkinson's disease. Nat Neurosci 14:85-92.

Chang RB, Strochlic DE, Williams EK, Umans BD, Liberles SD (2015) Vagal Sensory Neuron Subtypes that Differentially Control Breathing. Cell 161:622-633.

Chen YJ, Friedman BA, Ha C, Durinck S, Liu J, Rubenstein JL, Seshagiri S, Modrusan Z (2017) Single-cell RNA sequencing identifies distinct mouse medial ganglionic eminence cell types. Sci Rep 7:45656.

Clayton KK, Williamson RS, Watanabe Y, Hancock KE, Tasaka G-i, Mizrahi A, Hackett T, Polley DB (2020) Motor corollary discharge activates layer six circuits in the auditory cortex. bioRxiv:2020.2005.2028.121459.

Connelly WM, Schulz JM, Lees G, Reynolds JN (2010) Differential short-term plasticity at convergent inhibitory synapses to the substantia nigra pars reticulata. J Neurosci 30:14854-14861.

Daigle TL et al. (2018) A Suite of Transgenic Driver and Reporter Mouse Lines with Enhanced Brain-Cell-Type Targeting and Functionality. Cell 174:465-480 e422.

Dehorter N, Ciceri G, Bartolini G, Lim L, del Pino I, Marin O (2015) Tuning of fast-spiking interneuron properties by an activity-dependent transcriptional switch. Science 349:1216-1220.

DeLong MR (1971) Activity of pallidal neurons during movement. J Neurophysiol 34:414-427.

DeLong MR (1990) Primate models of movement disorders of basal ganglia origin. Trends Neurosci 13:281-285.

DeLong MR, Wichmann T (2007) Circuits and circuit disorders of the basal ganglia. Arch Neurol 64:20-24.

DeLong MR, Alexander GE, Georgopoulos AP, Crutcher MD, Mitchell SJ, Richardson RT (1984) Role of basal ganglia in limb movements. Hum Neurobiol 2:235-244.

Desmurget M, Turner RS (2010) Motor sequences and the basal ganglia: kinematics, not habits. J Neurosci 30:7685-7690.

Dodson PD, Larvin JT, Duffell JM, Garas FN, Doig NM, Kessaris N, Duguid IC, Bogacz R, Butt SJ, Magill PJ (2015) Distinct developmental origins manifest in the specialized encoding of movement by adult neurons of the external globus pallidus. Neuron 86:501-513.

Duan X, Krishnaswamy A, De la Huerta I, Sanes JR (2014) Type II cadherins guide assembly of a direction-selective retinal circuit. Cell 158:793-807.

Dudman JT, Krakauer JW (2016) The basal ganglia: from motor commands to the control of vigor. Curr Opin Neurobiol 37:158-166.

Eagle DM, Baunez C, Hutcheson DM, Lehmann O, Shah AP, Robbins TW (2008) Stop-signal reaction-time task performance: role of prefrontal cortex and subthalamic nucleus. Cereb Cortex 18:178-188.

Evans R, Twedell E, Zhu M, Ascencio J, Zhang R, Khaliq Z (2019) Functional dissection of basal ganglia inhibitory input onto SNc dopaminergic neurons. bioRxiv:856617.

Fife KH, Gutierrez-Reed NA, Zell V, Bailly J, Lewis CM, Aron AR, Hnasko TS (2017) Causal role for the subthalamic nucleus in interrupting behavior. Elife 6.

Filion M, Tremblay L, Bedard PJ (1991) Effects of dopamine agonists on the spontaneous activity of globus pallidus neurons in monkeys with MPTP-induced parkinsonism. Brain Res 547:152-161.

Fishell G, Kepecs A (2020) Interneuron Types as Attractors and Controllers. Annu Rev Neurosci 43:1-30.

Flandin P, Kimura S, Rubenstein JL (2010) The progenitor zone of the ventral medial ganglionic eminence requires Nkx2-1 to generate most of the globus pallidus but few neocortical interneurons. J Neurosci 30:2812-2823.

Fobbs WC, Bariselli S, Licholai JA, Miyazaki NL, Matikainen-Ankney BA, Creed MC, Kravitz AV (2020) Continuous Representations of Speed by Striatal Medium Spiny Neurons. J Neurosci 40:1679-1688.

Fox CA, Andrade AN, Lu Qui IJ, Rafols JA (1974) The primate globus pallidus: a Golgi and electron microscopic study. J Hirnforsch 15:75-93.

Fujiyama F, Nakano T, Matsuda W, Furuta T, Udagawa J, Kaneko T (2016) A single-neuron tracing study of arkypallidal and prototypic neurons in healthy rats. Brain Struct Funct 221:4733-4740.

Fujiyama F, Sohn J, Nakano T, Furuta T, Nakamura KC, Matsuda W, Kaneko T (2011) Exclusive and common targets of neostriatofugal projections of rat striosome neurons: a single neuron-tracing study using a viral vector. Eur J Neurosci 33:668-677.

Garas FN, Shah RS, Kormann E, Doig NM, Vinciati F, Nakamura KC, Dorst MC, Smith Y, Magill PJ, Sharott A (2016) Secretagogin expression delineates functionally-specialized populations of striatal parvalbumin-containing interneurons. Elife 5.

Gelman D, Griveau A, Dehorter N, Teissier A, Varela C, Pla R, Pierani A, Marin O (2011) A wide diversity of cortical GABAergic interneurons derives from the embryonic preoptic area. J Neurosci 31:16570-16580.

Giovanniello J, Yu K, Furlan A, Nachtrab GT, Sharma R, Chen X, Li B (2020) A central amygdala-globus pallidus circuit conveys unconditioned stimulus information and controls fear learning. bioRxiv:2020.2004.2028.066753.

Glajch KE, Kelver DA, Hegeman DJ, Cui Q, Xenias HS, Augustine EC, Hernandez VM, Verma N, Huang TY, Luo M, Justice NJ, Chan CS (2016) Npas1+ Pallidal Neurons Target Striatal Projection Neurons. J Neurosci 36:5472-5488.

Graybiel AM (2008) Habits, rituals, and the evaluative brain. Annu Rev Neurosci 31:359-387.

Graybiel AM, Aosaki T, Flaherty AW, Kimura M (1994) The basal ganglia and adaptive motor control. Science 265:1826-1831.

Grillner S, Robertson B (2016) The Basal Ganglia Over 500 Million Years. Curr Biol 26:R1088-R1100.

Grofova I (1975) The identification of striatal and pallidal neurons projecting to substantia nigra. An experimental study by means of retrograde axonal transport of horseradish peroxidase. Brain Res 91:286-291.

Hama H, Kurokawa H, Kawano H, Ando R, Shimogori T, Noda H, Fukami K, Sakaue-Sawano A, Miyawaki A (2011) Scale: a chemical approach for fluorescence imaging and reconstruction of transparent mouse brain. Nat Neurosci 14:1481-1488.

Hamani C, Saint-Cyr JA, Fraser J, Kaplitt M, Lozano AM (2004) The subthalamic nucleus in the context of movement disorders. Brain 127:4-20.

750 Hegeman DJ, Hong ES, Hernandez VM, Chan CS (2016) The external globus pallidus: progress and perspectives. Eur J Neurosci 43:1239-1265.

Hernandez VM, Hegeman DJ, Cui Q, Kelver DA, Fiske MP, Glajch KE, Pitt JE, Huang TY, Justice NJ, Chan CS (2015) Parvalbumin+ Neurons and Npas1+ Neurons Are Distinct Neuron Classes in the Mouse External Globus Pallidus. J Neurosci 35:11830-11847.

755 Higgs MH, Wilson CJ (2016) Unitary synaptic connections among substantia nigra pars reticulata neurons. J Neurophysiol 115:2814-2829.

Hodge RD et al. (2019) Conserved cell types with divergent features in human versus mouse cortex. Nature 573:61-68.

Hu JS, Vogt D, Sandberg M, Rubenstein JL (2017) Cortical interneuron development: a tale of time and space.
760 Development 144:3867-3878.

Huang ZJ, Paul A (2019) The diversity of GABAergic neurons and neural communication elements. Nat Rev Neurosci 20:563-572.

Hunt AJ, Jr., Dasgupta R, Rajamanickam S, Jiang Z, Beierlein M, Chan CS, Justice NJ (2018) Paraventricular hypothalamic and amygdalar CRF neurons synapse in the external globus pallidus. Brain Struct Funct
765 223:2685-2698.

Hutchison WD, Lozano AM, Davis KD, Saint-Cyr JA, Lang AE, Dostrovsky JO (1994) Differential neuronal activity in segments of globus pallidus in Parkinson's disease patients. Neuroreport 5:1533-1537.

Jaeger D, Kita H (2011) Functional connectivity and integrative properties of globus pallidus neurons. Neuroscience 198:44-53.

770 Jahanshahi M, Obeso I, Rothwell JC, Obeso JA (2015) A fronto-striato-subthalamic-pallidal network for goal-directed and habitual inhibition. Nat Rev Neurosci 16:719-732.

Jessell TM, Emson PC, Paxinos G, Cuello AC (1978) Topographic projections of substance P and GABA pathways in the striato- and pallido-nigral system: a biochemical and immunohistochemical study. Brain Res 152:487-498.

Jiang X, Shen S, Cadwell CR, Berens P, Sinz F, Ecker AS, Patel S, Tolias AS (2015) Principles of connectivity among morphologically defined cell types in adult neocortex. Science 350:aac9462.

Jin X, Tecuapetla F, Costa RM (2014) Basal ganglia subcircuits distinctively encode the parsing and concatenation of action sequences. Nat Neurosci 17:423-430.

Karube F, Takahashi S, Kobayashi K, Fujiyama F (2019) Motor cortex can directly drive the globus pallidus neurons in a projection neuron type-dependent manner in the rat. Elife 8.

Kawaguchi Y, Wilson CJ, Emson PC (1990) Projection subtypes of rat neostriatal matrix cells revealed by intracellular injection of biocytin. J Neurosci 10:3421-3438.

Ketzef M, Silberberg G (2020) Differential Synaptic Input to External Globus Pallidus Neuronal Subpopulations In Vivo. bioRxiv:2020.2002.2027.967869.

Kita H (1994) Parvalbumin-immunopositive neurons in rat globus pallidus: a light and electron microscopic study. Brain Res 657:31-41.

Kita H (2007) Globus pallidus external segment. Prog Brain Res 160:111-133.

Kita H, Kitai ST (1994) The morphology of globus pallidus projection neurons in the rat: an intracellular staining study. Brain Res 636:308-319.

Klaus A, Alves da Silva J, Costa RM (2019) What, If, and When to Move: Basal Ganglia Circuits and Self-Paced Action Initiation. Annu Rev Neurosci 42:459-483.

Klaus A, Martins GJ, Paixao VB, Zhou P, Paninski L, Costa RM (2017) The Spatiotemporal Organization of the Striatum Encodes Action Space. Neuron 95:1171-1180 e1177.

Kornhuber HH (1971) Motor functions of cerebellum and basal ganglia: the cerebellocortical saccadic (ballistic) clock, the cerebellonuclear hold regulator, and the basal ganglia ramp (voluntary speed smooth movement) generator. Kybernetik 8:157-162.

Krzywinski M, Altman N (2014) Visualizing samples with box plots. Nat Methods 11:119-120.

Levesque M, Parent A (2005) The striatofugal fiber system in primates: a reevaluation of its organization based on single-axon tracing studies. Proc Natl Acad Sci U S A 102:11888-11893.

Leys C, Ley C, Klein O, Bernard P, Licata L (2013) Detecting outliers: Do not use standard deviation around the mean, use absolute deviation around the median. Journal of Experimental Social Psychology 49:764-766.

Lim L, Mi D, Llorca A, Marin O (2018) Development and Functional Diversification of Cortical Interneurons. Neuron 100:294-313.

Madisen L, Zwingman TA, Sunkin SM, Oh SW, Zariwala HA, Gu H, Ng LL, Palmiter RD, Hawrylycz MJ, Jones AR, Lein ES, Zeng H (2010) A robust and high-throughput Cre reporting and characterization system for the whole mouse brain. Nat Neurosci 13:133-140.

Magill PJ, Bolam JP, Bevan MD (2001) Dopamine regulates the impact of the cerebral cortex on the subthalamic nucleus-globus pallidus network. Neuroscience 106:313-330.

Mahadevan V, Mitra A, Zhang Y, Peltekian A, Chittajallu R, Esnault C, Maric D, Rhodes C, Pelkey KA, Dale R, Petros TJ, McBain CJ (2020) NMDAR-mediated transcriptional control of gene expression in the specification of interneuron subtype identity. bioRxiv:2020.2006.2010.144295.

Mallet N, Pogosyan A, Marton LF, Bolam JP, Brown P, Magill PJ (2008) Parkinsonian beta oscillations in the external globus pallidus and their relationship with subthalamic nucleus activity. J Neurosci 28:14245-14258.

Mallet N, Schmidt R, Leventhal D, Chen F, Amer N, Boraud T, Berke JD (2016) Arkypallidal Cells Send a Stop Signal to Striatum. Neuron 89:308-316.

Markowitz JE, Gillis WF, Beron CC, Neufeld SQ, Robertson K, Bhagat ND, Peterson RE, Peterson E, Hyun M, Linderman SW, Sabatini BL, Datta SR (2018) The Striatum Organizes 3D Behavior via Moment-to-Moment Action Selection. Cell 174:44-58 e17.

Mastro KJ, Bouchard RS, Holt HA, Gittis AH (2014) Transgenic mouse lines subdivide external segment of the globus pallidus (GPe) neurons and reveal distinct GPe output pathways. J Neurosci 34:2087-2099.

Mastro KJ, Zitelli KT, Willard AM, Leblanc KH, Kravitz AV, Gittis AH (2017) Cell-specific pallidal intervention induces long-lasting motor recovery in dopamine-depleted mice. Nat Neurosci 20:815-823.

Mathis A, Yüksekgönül M, Rogers B, Bethge M, Mathis MW (2019) Pretraining boosts out-of-domain robustness for pose estimation. In, p arXiv:1909.11229.

Mathis A, Mamidanna P, Cury KM, Abe T, Murthy VN, Mathis MW, Bethge M (2018) DeepLabCut: markerless pose estimation of user-defined body parts with deep learning. Nat Neurosci 21:1281-1289.

Metsalu T, Vilo J (2015) ClustVis: a web tool for visualizing clustering of multivariate data using Principal Component Analysis and heatmap. Nucleic Acids Res 43:W566-570.

Mink JW (1996) The basal ganglia: focused selection and inhibition of competing motor programs. Prog Neurobiol 50:381-425.

Nambu A (2011) Somatotopic organization of the primate Basal Ganglia. Front Neuroanat 5:26.

Nambu A, Llinas R (1997) Morphology of globus pallidus neurons: its correlation with electrophysiology in guinea pig brain slices. J Comp Neurol 377:85-94.

Nath T, Mathis A, Chen AC, Patel A, Bethge M, Mathis MW (2019) Using DeepLabCut for 3D markerless pose estimation across species and behaviors. Nat Protoc 14:2152-2176.

Nelson AB, Kreitzer AC (2014) Reassessing models of basal ganglia function and dysfunction. Annu Rev Neurosci 37:117-135.

Nilsson SR, Goodwin NL, Choong JJ, Hwang S, Wright HR, Norville ZC, Tong X, Lin D, Bentzley BS, Eshel N, McLaughlin RJ, Golden SA (2020) Simple Behavioral Analysis (SimBA) – an open source toolkit for computer classification of complex social behaviors in experimental animals. bioRxiv:2020.2004.2019.049452.

Nini A, Feingold A, Slovin H, Bergman H (1995) Neurons in the globus pallidus do not show correlated activity in the normal monkey, but phase-locked oscillations appear in the MPTP model of parkinsonism. J Neurophysiol 74:1800-1805.

Nobrega-Pereira S, Gelman D, Bartolini G, Pla R, Pierani A, Marin O (2010) Origin and molecular specification of globus pallidus neurons. J Neurosci 30:2824-2834.

Nuzzo RL (2016) The Box Plots Alternative for Visualizing Quantitative Data. PM R 8:268-272.

Pamukcu A, Cui Q, Xenias HS, Berceau BL, Augustine EC, Fan I, Chalasani S, Hantman AW, Lerner TN, Boca SM, Chan CS (2020) Parvalbumin⁺ and Npas1⁺ Pallidal Neurons Have Distinct Circuit Topology and Function. bioRxiv:2020.2002.2014.950006.

Park J, Coddington LT, Dudman JT (2020) Basal Ganglia Circuits for Action Specification. Annual Review of Neuroscience 43:485-507.

Pollak Dorocic I, Furth D, Xuan Y, Johansson Y, Pozzi L, Silberberg G, Carlen M, Meletis K (2014) A whole-brain atlas of inputs to serotonergic neurons of the dorsal and median raphe nuclei. Neuron 83:663-678.

Poulin JF, Luppi MP, Hofer C, Caronia G, Hsu PK, Chan CS, Awatramani R (2020) PRISM: A Progenitor-Restricted Intersectional Fate Mapping Approach Redefines Forebrain Lineages. Dev Cell 53:740-753 e743.

Raz A, Vaadia E, Bergman H (2000) Firing patterns and correlations of spontaneous discharge of pallidal neurons in the normal and the tremulous 1-methyl-4-phenyl-1,2,3,6-tetrahydropyridine vervet model of parkinsonism. J Neurosci 20:8559-8571.

Redgrave P, Rodriguez M, Smith Y, Rodriguez-Oroz MC, Lehericy S, Bergman H, Agid Y, DeLong MR, Obeso JA (2010) Goal-directed and habitual control in the basal ganglia: implications for Parkinson's disease. Nat Rev Neurosci 11:760-772.

Romanelli P, Esposito V, Schaal DW, Heit G (2005) Somatotopy in the basal ganglia: experimental and clinical evidence for segregated sensorimotor channels. Brain Res Brain Res Rev 48:112-128.

Rothblat DS, Schneider JS (1995) Alterations in pallidal neuronal responses to peripheral sensory and striatal stimulation in symptomatic and recovered parkinsonian cats. Brain Res 705:1-14.

Rueda-Orozco PE, Robbe D (2015) The striatum multiplexes contextual and kinematic information to constrain motor habits execution. Nat Neurosci 18:453-460.

Sadek AR, Magill PJ, Bolam JP (2007) A single-cell analysis of intrinsic connectivity in the rat globus pallidus. J Neurosci 27:6352-6362.

Sandler M, Howard A, Zhu M, Zhmoginov A, Chen L-C (2018) MobileNetV2: Inverted Residuals and Linear Bottlenecks. In, p arXiv:1801.04381.

Sato F, Lavallee P, Levesque M, Parent A (2000) Single-axon tracing study of neurons of the external segment of the globus pallidus in primate. J Comp Neurol 417:17-31.

Saunders A, Oldenburg IA, Berezovskii VK, Johnson CA, Kingery ND, Elliott HL, Xie T, Gerfen CR, Sabatini BL (2015) A direct GABAergic output from the basal ganglia to frontal cortex. Nature 521:85-89.

Saunders A, Macosko EZ, Wysoker A, Goldman M, Krienen FM, de Rivera H, Bien E, Baum M, Bortolin L, Wang S, Goeva A, Nemesh J, Kamitaki N, Brumbaugh S, Kulp D, McCarroll SA (2018) Molecular Diversity and Specializations among the Cells of the Adult Mouse Brain. Cell 174:1015-1030 e1016.

Scardoni G, Petterlini M, Laudanna C (2009) Analyzing biological network parameters with CentiScaPe. Bioinformatics 25:2857-2859.

Schindelin J, Arganda-Carreras I, Frise E, Kaynig V, Longair M, Pietzsch T, Preibisch S, Rueden C, Saalfeld S, Schmid B, Tinevez JY, White DJ, Hartenstein V, Eliceiri K, Tomancak P, Cardona A (2012) Fiji: an open-source platform for biological-image analysis. Nat Methods 9:676-682.

Schmidt R, Leventhal DK, Mallet N, Chen F, Berke JD (2013) Canceling actions involves a race between basal ganglia pathways. Nat Neurosci 16:1118-1124.

Schwarz LA, Miyamichi K, Gao XJ, Beier KT, Weissbourd B, DeLoach KE, Ren J, Ibanes S, Malenka RC, Kremer EJ, Luo L (2015) Viral-genetic tracing of the input-output organization of a central noradrenaline circuit. Nature 524:88-92.

Schweizer N, Pupe S, Arvidsson E, Nordenankar K, Smith-Anttila CJ, Mahmoudi S, Andren A, Dumas S, Rajagopalan A, Levesque D, Leao RN, Wallen-Mackenzie A (2014) Limiting glutamate transmission in a Vglut2-expressing subpopulation of the subthalamic nucleus is sufficient to cause hyperlocomotion. Proc Natl Acad Sci U S A 111:7837-7842.

Shannon P, Markiel A, Ozier O, Baliga NS, Wang JT, Ramage D, Amin N, Schwikowski B, Ideker T (2003) Cytoscape: a software environment for integrated models of biomolecular interaction networks. Genome Res 13:2498-2504.

Shi LH, Luo F, Woodward DJ, Chang JY (2004) Neural responses in multiple basal ganglia regions during spontaneous and treadmill locomotion tasks in rats. Exp Brain Res 157:303-314.

Silberberg SN, Taher L, Lindtner S, Sandberg M, Nord AS, Vogt D, McKinsey GL, Hoch R, Pattabiraman K, Zhang D, Ferran JL, Rajkovic A, Golonzhka O, Kim C, Zeng H, Puelles L, Visel A, Rubenstein JLR (2016) Subpallial Enhancer Transgenic Lines: a Data and Tool Resource to Study Transcriptional Regulation of GABAergic Cell Fate. Neuron 92:59-74.

Smith Y, Bevan MD, Shink E, Bolam JP (1998) Microcircuitry of the direct and indirect pathways of the basal ganglia. Neuroscience 86:353-387.

Sousa VH, Fishell G (2010) Sonic hedgehog functions through dynamic changes in temporal competence in the developing forebrain. Curr Opin Genet Dev 20:391-399.

Streit M, Gehlenborg N (2014) Bar charts and box plots. Nat Methods 11:117.

Sztainberg Y, Kuperman Y, Justice N, Chen A (2011) An anxiolytic role for CRF receptor type 1 in the globus pallidus. J Neurosci 31:17416-17424.

Tasic B et al. (2016) Adult mouse cortical cell taxonomy revealed by single cell transcriptomics. Nat Neurosci 19:335-346.

Tasic B et al. (2018) Shared and distinct transcriptomic cell types across neocortical areas. Nature 563:72-78.

Turner RS, Anderson ME (1997) Pallidal discharge related to the kinematics of reaching movements in two dimensions. J Neurophysiol 77:1051-1074.

Turner RS, Anderson ME (2005) Context-dependent modulation of movement-related discharge in the primate globus pallidus. J Neurosci 25:2965-2976.

Turner RS, Grafton ST, Votaw JR, Delong MR, Hoffman JM (1998) Motor subcircuits mediating the control of movement velocity: a PET study. J Neurophysiol 80:2162-2176.

Verhulst A (1976) Tunga penetrans (Sarcopsylla penetrans) as a cause of agalactia in sows in the Republic of Zaire. Vet Rec 98:384.

Wallace ML, Saunders A, Huang KW, Philson AC, Goldman M, Macosko EZ, McCarroll SA, Sabatini BL (2017) Genetically Distinct Parallel Pathways in the Entopeduncular Nucleus for Limbic and Sensorimotor Output of the Basal Ganglia. Neuron 94:138-152 e135.

Wessel JR, Aron AR (2017) On the Globality of Motor Suppression: Unexpected Events and Their Influence on Behavior and Cognition. Neuron 93:259-280.

Wu Y, Richard S, Parent A (2000) The organization of the striatal output system: a single-cell juxtacellular labeling study in the rat. Neurosci Res 38:49-62.

Yao Z et al. (2020) A taxonomy of transcriptomic cell types across the isocortex and hippocampal formation. bioRxiv:2020.2003.2030.015214.

Yttri EA, Dudman JT (2016) Opponent and bidirectional control of movement velocity in the basal ganglia. Nature 533:402-406.

Yuan XS, Wang L, Dong H, Qu WM, Yang SR, Cherasse Y, Lazarus M, Schiffmann SN, d'Exaerde AK, Li RX, Huang ZL (2017) Striatal adenosine A2A receptor neurons control active-period sleep via parvalbumin neurons in external globus pallidus. Elife 6.

Figure Legends

935 **Figure 1. Novel markers and driver lines for interrogating GPe neurons.**

a. Left, Single-cell transcriptomic data identified four distinct clusters of GPe neurons; these include Npas1$^+$-Foxp2$^+$ (blue, 10 o'clock), Npas1$^+$-Nkx2.1$^+$(cyan, 7 o'clock), and two subpopulations of PV$^+$ neurons (red and teal, 6 o'clock). Right, Npy2r is expressed in all non-Npas1$^+$-Foxp2$^+$ neurons; Npr3 and Kcng4 are expressed in a select subset of Npas1$^+$ neurons and PV$^+$ neurons, respectively. Figure adapted from (Saunders et al., 2018). Original expression

940 data can be viewed at http://dropviz.org/?_state_id_=6c13807c8420bc74.

b. Sagittal brain sections showing the *in situ* hybridization signals for Npr3 (left), Kcng4 (middle), Npy2r (right) in the GPe and neighboring areas. Data were adapted from Allen Brain Atlas. Brightness and contrast were adjusted. Raw data can be viewed and downloaded from http://mouse.brain-map.org.

c. Top left, Coexpression (dotted circle) of Npas1(blue) but not Foxp2 (green) in Npr3$^+$ neurons (magenta). Npas1$^+$-

945 Foxp2$^+$ (and non-Npr3$^+$) neurons were visible in the same field (arrowheads). Middle left, Coexpression (dotted circle) of Npas1(blue) and Nkx2.1 (magenta) in Npr3$^+$ neurons (green). Npas1$^+$ neurons that non-Nkx2.1$^+$ and non-Npr3$^+$ were visible in the same field (arrowheads). Bottom left, Coexpression (dotted circle) of PV (green) in Kcng4$^+$ neurons (magenta). Top right, Npr3$^+$ neurons share axonal projection patterns similar to that of Npas1$^+$-Nkx2.1$^+$; strong axonal projection to the cortex (Ctx), thalamic reticular nucleus (TRN), and substantia nigra pars compacta

950 (SNc) was evident. Projections were assessed using viral delivery of ChR2-eYFP. Bottom right, virally delivered synaptophysin-GFP in Kcng4-Cre mice revealed near-exclusive axonal projection from the external globus pallidus (GPe) to the subthalamic nucleus (STN) and substantia nigra pars reticulata (SNr). Abbreviations: dStr = dorsal striatum.

d. Using HuCD as a neuronal marker, population data for the relative abundance of GPe neuron markers were

955 determined. Each circle represents a section. Medians and sample sizes are: Sox6$^+$ (63.7%, 14), Npy2r$^+$ (63.4%, 3), Nkx2.1$^+$ (59.6%, 16), PV$^+$ (49.2%, 19), Lhx6$^+$ (33.7%, 12), Npas1$^+$ (32.2%, 21), Foxp2$^+$ (22.1%, 10), Npr3$^+$ (14.0%, 4), Kcng4$^+$ (10.8%, 6), Dbx1$^+$ (9.0%, 22), ChAT$^+$ (5.9%, 9). Data are ranked based on the median values as denoted by the thick lines. Parts of the data have been previously published.

960 **Figure 2. Npy2r-Cre mice capture a mixed population of GPe neurons.**

a. Npy2r-L-tdTomato mice labeled neurons in the GPe and striosomes in the dorsal striatum (dStr) (top). Inset, a magnified view of a striosome. Prominent axons were apparent in the subthalamic nucleus (STN) (middle) and substantial nigra pars compacta (SNc) and reticulata (SNr) (bottom).

b. Axonal projection patterns from Npy2r$^+$ neurons are similar to that of Npas1$^+$-Nkx2.1$^+$ neurons and Npr3$^+$ neurons. Only a low density of axons was observed in the subthalamic nucleus (STN) and substantial nigra pars reticulata (SNr). Lower right, ChR2-eYFP$^+$ neurons were largely Npas1$^+$.

c. Top left, tdTomato-expressing (PV$^+$-Npy2r$^+$) neurons were observed throughout the GPe in PV-Npy2r-FL-tdTomato mice. PV$^+$-Npy2r$^+$ neurons were immunoreactive for Nkx2.1 (top right) but not for Npas1 (middle right). Bottom, most of PV$^+$-Npy2r$^+$ (tdTomato$^+$) neurons were PV$^+$. PV$^+$-Npy2r$^-$ (green) neurons were visible in the same field (arrowheads).

d. A composite confocal micrograph showing a typical biocytin-filled PV$^+$-Npy2r$^+$ neuron. In addition to the main axon, local collaterals were observed.

Abbreviations: cc = corpus callosum; dStr = dorsal striatum; ic = internal capsule; MO = motor cortex; SubB = subbrachial nucleus; TRN = thalamic reticular nucleus; ZI = zona incerta.

Figure 3. GPe neurons display graded electrophysiology attributes.

Scatter plot summary of the electrophysiological properties of identified GPe neuron subtypes. Max current (**a**), max rate (**b**), trough potential (**c**), spontaneous rate (**d**), 1st/last ISI ratio (**e**), sag ratio (**f**), CV_{ISI} (**g**), spike width (**h**), membrane potential (**i**), and 1st spike height (**j**) are shown. See **Table 1** & **2** for a listing of median values, sample sizes, and statistical analysis of new neuron types, as compared to our recent publication (Abecassis et al., 2020), along with PV$^+$ neurons and Npas1$^+$ neurons for comparison. The data are ordered according to their median value as indicated by the thick vertical lines. Each cell is shown as a circle. A total of 329 neurons were included (n = Dbx1$^+$: 24, Foxp2$^+$: 16, Kcng4$^+$: 20, Lhx6$^+_{bright}$: 24, Lhx6$^+_{dim}$: 10, Lhx6$^+_{pan}$: 68, Npas1$^+$: 24, Npas1$^+$-Lhx6$^+$: 14, Npr3$^+$: 9, Npy2r$^+$: 12, PV$^+$: 41, PV$^+$-Dbx1$^+$: 21, PV$^+$-Lhx6$^+$: 14, PV$^+$-Npy2r$^+$: 32) in this analysis. The complete dataset for electrophysiological measurements of the intrinsic properties and an interactive web tool can be found online: https://graceyichen.shinyapps.io/neuro_interactive_analysis/.

990 **Figure 4. Clustering and network analysis of electrophysiological attributes.**

a. Left, Heatmap representation of electrical signatures of genetically-identified GPe neuron subtypes. Dendrograms show the order and distances of neuron clusters and their electrical characteristics. A total of 212 neurons (*n* = Dbx1$^+$: 20, Foxp2$^+$: 16, Kcng4$^+$: 13, Lhx6$^+_{bright}$: 18, Lhx6$^+_{dim}$: 7, PV$^+$: 38, PV$^+$-Dbx1$^+$: 16, PV$^+$-Lhx6$^+$: 12, PV$^+$-Npy2r$^+$: 21, Npas1$^+$: 19, Npas1$^+$-Lhx6$^+$: 13, Npr3$^+$: 8, Npy2r$^+$: 10) were included in this analysis. Neurons with
995 incomplete data were excluded from the analysis. Two main clusters were identified; cluster 1 contains 87 cells, cluster 2 contains 125 cells. Right, genetically-defined PV$^+$ neurons are re-clustered. Scale bar applies to both panels. Purple-red-yellow colors were assigned for Npas1$^+$ neurons, blue-green colors were assigned for PV$^+$ neurons, and grays were used for mixed neuron types (i.e., Dbx1$^+$ and Npy2r$^+$).

b. t-SNE analysis of the same data set as **a** yielded two distinct clusters. Cluster 1 (light gray) contains 88 cells,
1000 cluster 2 (dark gray) contains 124 cells. The membership assignment in cluster 1 and 2 for each neuron subtypes are as follows: Foxp2$^+$ (100.0%, 0.0%), Npas1$^+$ (95.2%, 4.8%), Lhx6$^+_{bright}$ (94.4%, 5.6%), Npr3$^+$ (87.5%, 12.5%), Dbx1$^+$ (30.0%, 70.0%), Npy2r$^+$(30.0%, 70.0%), PV$^+$-Lhx6$^+$ (25.0%, 75.0%), Lhx6$^+_{dim}$ (14.3%, 85.7%), PV$^+$-Dbx1$^+$ (12.5%, 87.5%), PV$^+$ (5.3%, 94.7%), PV$^+$-Npy2r$^+$ (4.8%, 95.2%), and Kcng4$^+$ (0.0%, 100.0%).

c. Principal component biplot showing the relative contributions of each electrophysiological attribute to PC1 and
1005 PC2. Markers represent the centroids for each cell type. The length of each vector is proportional to its variance with the cosine of the angle made by the vector with each axis indicating its contribution to that principal component. Highly correlated variables have similar directions; uncorrelated variables are perpendicular to each other.

d. Partial correlation networks with a spring layout from all cells (top), PV$^+$ neurons (middle), and Npas1$^+$ neurons
1010 (bottom). Inset, bootstrap of edge stability. The size of the gray circles represents the connectivity of nodes to each other as measured by closeness centrality index. Edge thickness indicates the correlation between nodes. Colors indicate the polarity of correlations.

Figure 5. Markerless tracking and behavioral dynamics.

1015 **a**. Top left, A still frame showing a mouse exploring in an open-field arena. Patch cords were attached to the fiber implants for optogenetic interrogation. Color circles represent pose estimation markers. Top right, A magnified view of the same mouse shown on the left. Eight body parts were labeled and used for tracking body kinematics and motor patterns. Angle (θ), width (w), and length (l) were measured. Bottom, A schematized labeling configuration is shown. Right, Four discrete motor behavior motifs were extracted, namely, locomotion, fine
1020 movement, motionless, and rearing.

b. The behavioral composition is shown as percent time spent. PV-Cre (n = 12) and Npas1-Cre (n = 16) mice virally transduced with ChR2-eYFP were included in this analysis. Mice were tethered to the patch cords but no light was delivered.

c. Left, Learning curves of the DeepLabCut network over five rounds of training. Additional annotated frames were
1025 incorporated into the dataset in each round. An initial steep and monotonic decrease in loss was followed by a steady plateau. A large amount of new data was added to round 5, resulting in a high loss initially. The same data from round 5 were replotted on a linear scale as an inset (top right). Middle, An X-Y scatter plot comparing the speeds measured using DeepLabCut vs. Ethovision. Each marker is a frame. Diagonal line represents unity (i.e., x = y). Right, Precision-recall curve of the SimBA rearing classifier. Arrow indicates the maxima for the F1 score
1030 (0.71).

d. Left & middle, Ethograms showing the motor dynamics of a PV-Cre mouse (left) and Npas1-Cre mouse (right) across 20 one-minute trials (columns). The beginning of each trial starts at the top of the plots. Square boxes show the time period in which light was delivered in the GPe. Rasters represent the occurrence of defined behavioral events: locomotion (gray), fine movement (green), rearing (light pink), and motionless (magenta). Each
1035 column is a single trial; twenty trials are shown for both PV-Cre and Npas1-Cre. Right, Population average changes in the event frequency of motionless, fine movement, rearing, and locomotion upon optogenetic stimulation (blue horizontal lines) of PV-Cre (n = 12, top) and Npas1-Cre (n = 16, bottom) mice transduced with ChR2-eYFP.

e. Top to bottom, Correlated changes in speed, length-width ratio, and body angle of an example mouse across time. Speed data (orange dotted lines) were filtered and scaled to facilitate comparisons.

1040 **f**. A correlation matrix constructed using time series data from both pre-period and light-period illustrating moment-to-moment covariance of the different movement metrics. The event frequencies of the four behaviors,

body angle, length-width ratio, and speed were used in this comparison. PV-Cre and Npas1-Cre mice (virally transduced with ChR2-eYFP) were included in this analysis (n = 28). Light colors indicate positive correlations; dark colors indicate negative correlations.

1045

Figure 6. Motor patterns of mice with cell-specific optogenetic stimulation.

a. Left, A correlation matrix constructed using data from PV-Cre (n = 12) and Npas1-Cre (n = 16) mice transduced with ChR2-eYFP. Eighteen parameters were included in this matrix. Blue colors indicate positive correlations, brown colors indicate negative correlations. Right, PCA plots showing the distributions of PV-Cre (dark gray, n = 1050 12) and Npas1-Cre (light gray, n = 16) mice (transduced with ChR2-eYFP) in pre-period (top) and light-period (bottom). Each marker represents a mouse. Twenty three movement metrics were used in this analysis.

b. A heatmap summarizing motor responses of mice to optogenetic stimulation of genetically-defined neurons in the GPe. Twenty-five movement metrics were measured to fully capture the behavioral structures. Each of the 25 rows represents the fold change of movement metrics. Warm colors (red) represent positive changes; cool colors 1055 (blue) represent negative changes. Rows and columns were sorted using hierarchical clustering. Dendrograms are divided into two main arms; metrics on the upper arm are negatively correlated with 'total frequency', while metrics on the lower arm are positively correlated with 'total frequency'. Each column is a mouse; 54 mice were used in this analysis. The neurons of interest are PV^+ (purple), $Npas1^+$ (green), $Kcng4^+$ (blue), and $Foxp2^+$ (red) neurons.

c. Plots showing the speed of mice with optogenetic stimulation in genetically-defined neurons in the GPe. Blue 1060 horizontal lines indicate the timing of light delivery. Thick lines indicate average, gray areas indicate standard error of the means.

d. Slopegraphs showing event frequency (counts per 10 s) for total, locomotion, fine movement, and motionless in mice and the effect with optogenetic stimulation of selective neuron types. Each connected line represents a mouse: PV^+ neurons (n = 12), $Npas1^+$ neurons (n = 16), $Kcng4^+$ neurons (n = 8), $Foxp2^+$ neurons (n = 18), dSPNs (n 1065 = 9), and iSPNs (n = 11).

e. Heatmaps showing the relative cumulative time that mice spent in each position following optogenetic stimulation of genetically-defined GPe neurons. Yellow represents more time spent; blue represents less time spent. Each heatmap was scaled to min and max and does not represent the net locomotor activity of mice. **f**. A

box plot summarizing the amount of time mice spent in the center of the area during pre- (black) and light-period
1070 (blue). PV^+ neurons (n = 12), $Npas1^+$ neurons (n = 16), $Kcng4^+$ neurons (n = 8), $Foxp2^+$ neurons (n = 18), dSPNs (n = 9), and iSPNs (n = 11).

Figure 7. Optogenetic manipulations produced cell-specific motor patterns.

a. A decision boundary matrix visualizing the relationships between movement metrics and how they would be
1075 classified if predicted through the current model. Boundaries between classes are visualized. All variables were scaled to have a mean of 0 and a standard deviation of 1.

b. Receiver operating characteristic (ROC) curves for different cell types are shown. Classifiers that give curves closer to the top-left corner indicate a better performance; the closer the curve comes to the diagonal of the ROC space, the less accurate the test.

1080 **c**. A magnified view of the relationships between two predictor pairs. Hashlines demarcate the origin, data associated with iSPNs are uniquely situated on the lower-left corner of the graph (see inset).

d. Left, A summary plot showing the mean and its 95% confidence interval for each of 23 variables for each of the two clusters. All variables were scaled. Right, t-SNE visualization of clustering. Cluster 1 (light gray) has a size of 26, whereas cluster 2 (dark gray) has a size of 30. Memberships for cluster 1: PV^+ pre = 41.7% (5/12); PV^+ light =
1085 75.0% (9/12); $Npas1^+$ pre = 56.3% (9/16); $Npas1^+$ light = 18.8% (3/16). Memberships for cluster 2: PV^+ pre = 58.3% (7/12); PV^+ light = 25.0% (3/12); $Npas1^+$ pre = 43.8% (7/16), $Npas1^+$ light = 81.3% (13/16).

Figure 8. Local collateral connectivity within the GPe is cell-specific.

a. An axon arborized locally in the vicinity of a biocytin-filled GPe neuron. Axons were identified as small-caliber
1090 processes that bear varicosities and contain no spines. Top right, an inset showing a series of varicosities produced by the biocytin-filled neuron. Bottom, Six additional examples of varicosities and their parent axons are shown.

b. Top, Inwardly-directed spontaneous inhibitory postsynaptic currents (IPSCs) were readily observed in voltage-clamped GPe neurons *ex vivo*. Large, periodic events were blocked by the application of tetrodotoxin (1 μM), a

1095 voltage-gated sodium channel blocker. Bottom, A histogram showing the IPSC amplitude distribution. Inset, Averaged miniature IPSCs (gray) and large (> 150 pA) IPSCs (black) are shown.

c. Top, A current trace showing periodic IPSCs recorded from a voltage-clamped GPe neuron. Bottom, An autocorrelation of the IPSC train from an example neuron with one unitary input, fitted with a sum of Gaussian components, indicating that the neuron received one periodic input in addition to aperiodic input (left). The 1100 waveform of the averaged unitary IPSC is shown (right). Right, A cumulative plot showing the difference in the amplitude distribution of periodic (black) and aperiodic events (gray).

d. Spontaneous IPSCs and optogenetically evoked IPSCs (arrows) were observed from a voltage-clamped PV^{-} neuron (V_{hold} = −30 mV). A low-chloride internal solution was used. Light stimuli (blue circle) were delivered asynchronously relative to the occurrence of spontaneous IPSCs. A proposed microcircuit is shown on the top.

1105 **e**. Top, Peri-stimulus time histogram (PSTH) and raster plot showing the occurrence of spontaneous IPSCs. Evoked IPSCs were excluded. Middle & bottom, an expanded time scale showing resetting the timing of spontaneous IPSCs. Periodicity is demonstrated by the evenly spaced peaks in the PSTH. No temporal structures in the spontaneous IPSCs were observed before light delivery.

f. Local connectivity was dissected using optogenetics *ex vivo*. Example traces from PV^{+} to PV^{-} (top), $Npas1^{+}$ to 1110 $Npas1^{-}$ (middle), and $Foxp2^{+}$ to PV^{+} (bottom) are shown. ChR2-eYFP negative neurons were targeted for recording. For positive identification of PV^{+} neurons, PV^{+} neurons were labeled with the PV-tdTom allele. Inset, Four connection types were examined: PV^{+} to PV^{-} (blush, n = 19), $Npas1^{+}$ to $Npas1^{-}$ (purple, n = 16), $Npas1^{+}$ to PV^{+} (green, n = 39), and $Foxp2^{+}$ to PV^{+} (olive, n = 18). The proportion of neurons that responded are shown as bar graphs. Only a subset of recorded PV^{+} neurons (8 out of 18, 44.4%) showed detectable $Foxp2^{+}$ input.

1115 **g**. Top, Population data showing IPSC amplitude for four different connection types across 50 pulses: PV^{+} to PV^{-} (blush, n = 19), $Npas1^{+}$ to $Npas1^{-}$ (purple, n = 15), $Npas1^{+}$ to PV^{+} (green, n = 39), and $Foxp2^{+}$ to PV^{+} (olive, n = 8). Each line represents median values. Bottom, univariate scatter plot showing the first IPSC amplitudes for four different connection types. Thick lines represent the medians. Whiskers represent interquartile ranges.

1120

Video Legends

Supplemental video. Machine learning approaches capture mouse behavior motifs in an open field. Representative movie of a mouse in an open field arena. Current behavior of the mouse is displayed. Event timers track the cumulative duration of locomotion, rearing, fine movement, and motionless events. Video is shown at 0.5x speed.

Table 1. Electrophysiological characteristics of GPe neurons.

	Kcng4⁺ neurons		Npas1⁺ neurons		Npas1⁺-Lhx6⁺ neurons		Npr3⁺ neurons		Npy2r⁺ neurons		PV⁺ neurons		PV⁺-Lhx6⁺ neurons		PV⁺-Npy2r⁺ neurons	
	Median ± MAD	n[a]	Median ± MAD	n	Median ± MAD	n	Median ± MAD	n	Median ± MAD	n	Median ± MAD	n	Median ± MAD	n	Median ± MAD	n
Spontaneous rate (Hz)	16.91 ± 2.82	14	8.43 ± 3.05	63	9.31 ± 2.83	30	6.63 ± 2.51	13	10.0 ± 3.42	11	16.69 ± 3.43	111	14.26 ± 3.18	16	14.95 ± 5.59	22
CV ISI	0.14 ± 0.03	14	0.27 ± 0.1	63	0.2 ± 0.06	30	0.19 ± 0.04	13	0.18 ± 0.08	11	0.14 ± 0.03	111	0.14 ± 0.04	16	0.13 ± 0.04	22
Max rate (Hz)	184.0 ± 16.0	20	96.0 ± 34.0	33	102.0 ± 22.0	14	92.0 ± 16.0	9	177.0 ± 36.0	12	198.0 ± 24.0	49	173.0 ± 24.0	14	188.0 ± 38.0	32
Max current (pA)	1120.0 ± 300.0	19	170.0 ± 90.0	24	460.0 ± 140.0	13	380.0 ± 40.0	9	1280.0 ± 300.0	12	1180.0 ± 260.0	41	800.0 ± 100.0	14	1100.0 ± 580.0	31
Membrane potential (mV)	−55.41 ± 3.23	20	−51.41 ± 2.96	24	−54.45 ± 1.92	14	−53.71 ± 1.77	9	−54.16 ± 1.7	12	−55.72 ± 2.56	41	−56.68 ± 2.06	14	−54.31 ± 5.0	32
Trough potential (mV)	−95.27 ± 4.54	20	−154.81 ± 17.26	24	−129.11 ± 16.88	30	−136.17 ± 7.78	9	−81.67 ± 10.4	12	−98.62 ± 6.35	41	−113.94 ± 18.65	14	−97.28 ± 16.76	32
Sag ratio	1.1 ± 0.03	20	1.35 ± 0.18	24	1.15 ± 0.09	30	1.2 ± 0.07	9	1.11 ± 0.06	12	1.1 ± 0.03	41	1.17 ± 0.1	14	1.15 ± 0.08	32
First/last ISI ratio	0.86 ± 0.02	20	0.61 ± 0.06	24	0.78 ± 0.02	14	0.73 ± 0.06	9	0.86 ± 0.03	12	0.8 ± 0.05	41	0.83 ± 0.03	14	0.84 ± 0.05	32
AP height (mV)	67.93 ± 7.33	20	63.44 ± 8.52	24	71.98 ± 5.26	14	72.44 ± 3.28	9	60.63 ± 3.39	12	67.08 ± 6.68	41	71.83 ± 7.45	14	66.26 ± 12.56	32
AP width (ms)	0.64 ± 0.05	20	1.11 ± 0.23	24	1.28 ± 0.17	14	0.99 ± 0.07	9	0.68 ± 0.08	12	0.67 ± 0.06	41	0.72 ± 0.1	14	0.62 ± 0.11	32

[a] n equal to the number of neurons.

AP, action potential; CV, coefficient of variation; ISI, interspike interval; MAD, median absolute deviation.

Table 2. Statistical analysis for electrophysiological characteristics

	Kruskal-Wallis [a]	Pairwise comparisons [b]													
		Kcng4$^+$ vs Npas1$^+$	Kcng4$^+$ vs Npas1$^+$-Lhx6$^+$	Kcng4$^+$ vs Npr3$^+$	Kcng4$^+$ vs Npr2$^+$	Kcng4$^+$ vs PV$^+$	Kcng4$^+$ vs PV$^+$-Lhx6$^+$	Kcng4$^+$ vs PV$^+$-Npy2r$^+$	Npas1$^+$ vs Npas1$^+$-Lhx6$^+$	Npas1$^+$ vs Npr3$^+$	Npas1$^+$ vs Npr2$^+$	Npas1$^+$ vs PV$^+$	Npas1$^+$ vs PV$^+$-Lhx6$^+$	Npas1$^+$ vs PV$^+$-Npy2r$^+$	Npas1$^+$-Lhx6$^+$ vs Npr3$^+$
Spontaneous activity (Hz)	**< 0.0001**	**0.0019**	**0.0037**	0.014	0.38	> 0.99	> 0.99	> 0.99	> 0.99	> 0.99	> 0.99	**< 0.0001**	0.057	**0.00010**	> 0.99
CV ISI	**< 0.0001**	0.014	0.97	> 0.99	> 0.99	> 0.99	> 0.99	> 0.99	> 0.99	> 0.99	> 0.99	**< 0.0001**	0.011	**< 0.0001**	> 0.99
Max rate (Hz)	**< 0.0001**	**< 0.0001**	**0.0014**	**0.0040**	> 0.99	> 0.99	> 0.99	> 0.99	> 0.99	> 0.99	**0.0029**	**< 0.0001**	0.0059	**< 0.0001**	> 0.99
Max current (pA)	**< 0.0001**	**< 0.0001**	0.046	0.019	> 0.99	> 0.99	> 0.99	> 0.99	> 0.99	> 0.99	**< 0.0001**	**< 0.0001**	0.022	**< 0.0001**	> 0.99
Membrane potential (mV)	0.26	> 0.99	> 0.99	> 0.99	> 0.99	> 0.99	> 0.99	> 0.99	> 0.99	> 0.99	> 0.99	> 0.99	0.38	0.79	> 0.99
Trough potential (mV)	**< 0.0001**	**< 0.0001**	**< 0.0001**	**0.0021**	> 0.99	> 0.99	0.38	> 0.99	> 0.99	> 0.99	**< 0.0001**	**< 0.0001**	0.072	**< 0.0001**	> 0.99
Sag ratio	**0.00011**	**0.00013**	> 0.99	> 0.99	> 0.99	> 0.99	> 0.99	0.99	0.022	> 0.99	0.10	**< 0.0001**	0.19	0.099	> 0.99
First/last IS ratio	**< 0.0001**	**< 0.0001**	0.028	**0.010**	> 0.99	0.019	> 0.99	> 0.99	0.40	> 0.99	**0.00036**	**0.0014**	**0.00031**	**< 0.0001**	> 0.99
AP height (mV)	0.036	> 0.99	> 0.99	> 0.99	> 0.99	> 0.99	> 0.99	> 0.99	> 0.99	> 0.99	> 0.99	> 0.99	> 0.99	> 0.99	> 0.99
AP width (ms)	**< 0.0001**	**< 0.0001**	**< 0.0001**	**0.0016**	> 0.99	> 0.99	> 0.99	> 0.99	> 0.99	> 0.99	0.0086	**< 0.0001**	**0.0041**	**< 0.0001**	> 0.99

	Pairwise comparisons [b]													
	Npas1$^+$-Lhx6$^+$ vs Npr2$^+$	Npas1$^+$-Lhx6$^+$ vs PV$^+$	Npas1$^+$-Lhx6$^+$ vs PV$^+$-Lhx6$^+$	Npas1$^+$-Lhx6$^+$ vs PV$^+$-Npy2r$^+$	Npr3$^+$ vs Npr2$^+$	Npr3$^+$ vs PV$^+$	Npr3$^+$ vs PV$^+$-Lhx6$^+$	Npr3$^+$ vs PV$^+$-Npy2r$^+$	Npy2r$^+$ vs PV$^+$	Npy2r$^+$ vs PV$^+$-Lhx6$^+$	Npy2r$^+$ vs PV$^+$-Npy2r$^+$	PV$^+$ vs PV$^+$-Lhx6$^+$	PV$^+$ vs PV$^+$-Npy2r$^+$	PV$^+$-Lhx6$^+$ vs PV$^+$-Npy2r$^+$
Spontaneous activity (Hz)	> 0.99	**< 0.0001**	0.081	**0.00050**	> 0.99	**< 0.0001**	0.16	**0.0050**	0.029	> 0.99	0.26	> 0.99	> 0.99	> 0.99
CV ISI	> 0.99	**0.0043**	> 0.99	0.020	> 0.99	0.98	> 0.99	0.68	> 0.99	> 0.99	> 0.99	> 0.99	> 0.99	> 0.99
Max rate (Hz)	0.053	**< 0.0001**	0.11	**< 0.0001**	0.067	**< 0.0001**	0.13	**0.00059**	> 0.99	> 0.99	> 0.99	> 0.99	> 0.99	> 0.99
Max current (pA)	0.095	**0.0018**	> 0.99	0.050	0.038	**0.0011**	> 0.99	0.022	> 0.99	> 0.99	> 0.99	0.30	> 0.99	> 0.99
Membrane potential (mV)	> 0.99	> 0.99	> 0.99	> 0.99	> 0.99	> 0.99	> 0.99	> 0.99	> 0.99	> 0.99	> 0.99	> 0.99	> 0.99	> 0.99
Trough potential (mV)	< 0.0001	**< 0.0001**	> 0.99	**0.00026**	**0.0015**	0.0067	> 0.99	0.016	> 0.99	0.21	> 0.99	> 0.99	> 0.99	> 0.99
Sag ratio	> 0.99	> 0.99	> 0.99	> 0.99	> 0.99	> 0.99	> 0.99	> 0.99	> 0.99	> 0.99	> 0.99	> 0.99	> 0.99	> 0.99
First/last IS ratio	> 0.99	> 0.99	> 0.99	0.28	0.64	> 0.99	0.79	0.090	> 0.99	> 0.99	> 0.99	> 0.99	0.28	> 0.99
AP height (mV)	0.47	> 0.99	> 0.99	> 0.99	0.33	0.75	> 0.99	> 0.99	> 0.99	0.30	> 0.99	0.61	> 0.99	> 0.99
AP width (ms)	**0.0043**	**< 0.0001**	**0.0023**	**< 0.0001**	0.27	0.0091	0.21	**0.00038**	> 0.99	> 0.99	> 0.99	> 0.99	> 0.99	> 0.99

Two-tailed P values are listed. [a] Kruskal–Wallis tests were performed to compare each characteristic across all groups. [b] Dunn tests were performed to compare each pair of neuron types. The bolded P values are significant when using a Bonferroni correction at a significance level of 0.05, adjusting for the fact that 10 characteristics were considered.

Table 3. Summary of optogenetic effects on behavior metrics

	PV⁺ neurons, ChR2 (n = 12)		Npas1⁺ neurons, ChR2 (n = 16)		Kcng4⁺ neurons, ChR2 (n = 8)		Foxp2⁺ neurons, ChR2 (n = 18)		STN neurons, ACR2 (n = 10)		dSPNs, ChR2 (n = 9)		iSPNs, ChR2 (n = 11)	
	Fold change	P value [c]	Fold change	P value	Fold change	P value	Fold change	P value	Fold change	P value	Fold change	P value	Fold change	P value
Speed (cm/s)	1.53 ± 0.31	0.00098	0.81 ± 0.09	**0.000031**	1.52 ± 0.33	0.0078	0.36 ± 0.12	**0.0000076**	1.68 ± 0.15	0.0020	1.9 ± 0.25	0.0039	0.52 ± 0.09	0.00098
Body length-width ratio	1.1 ± 0.05	0.00049	1.0 ± 0.05	**0.00015**	1.16 ± 0.08	0.023	0.88 ± 0.06	**0.000023**	1.19 ± 0.03	0.0020	1.14 ± 0.11	0.0039	0.97 ± 0.04	0.083
Total frequency [a]	0.71 ± 0.12	0.00049	1.08 ± 0.08	**0.000061**	0.79 ± 0.06	0.0078	1.36 ± 0.17	**0.000015**	0.68 ± 0.06	0.0020	0.76 ± 0.16	0.0039	1.12 ± 0.09	0.31
Locomotion frequency	0.78 ± 0.12	0.00049	1.1 ± 0.04	**0.000092**	0.82 ± 0.1	0.023	1.32 ± 0.18	**0.000076**	0.71 ± 0.05	0.0020	0.91 ± 0.18	0.20	0.9 ± 0.04	0.0098
Fine movement frequency	0.69 ± 0.12	0.00049	1.06 ± 0.1	**0.000061**	0.77 ± 0.13	0.0078	1.35 ± 0.21	**0.000015**	0.63 ± 0.08	0.0020	0.82 ± 0.14	0.0039	1.04 ± 0.08	0.81
Rearing frequency	0.91 ± 0.2	0.15	0.87 ± 0.18	0.026	0.98 ± 0.13	0.56	0.68 ± 0.31	0.00092	1.56 ± 0.33	0.0039	0.97 ± 0.32	0.97	0.29 ± 0.11	0.00098
Motionless frequency	0.5 ± 0.18	0.0015	1.03 ± 0.46	0.0011	0.67 ± 0.14	0.016	1.77 ± 0.34	0.0019	0.51 ± 0.13	0.0059	0.33 ± 0.14	0.0039	1.88 ± 0.34	0.00098
Locomotion % time	1.24 ± 0.09	0.0024	0.99 ± 0.07	0.0013	1.11 ± 0.04	0.0078	0.86 ± 0.06	0.0023	1.18 ± 0.13	0.0059	1.37 ± 0.12	0.0039	0.66 ± 0.1	0.0029
Fine movement % time	0.66 ± 0.14	0.00049	1.09 ± 0.14	**0.000031**	0.74 ± 0.16	0.0078	1.51 ± 0.32	**0.000038**	0.53 ± 0.12	0.0020	0.79 ± 0.13	0.0039	1.03 ± 0.08	0.64
Rearing % time	1.02 ± 0.25	0.91	0.82 ± 0.16	0.013	1.21 ± 0.14	0.023	0.54 ± 0.25	0.0010	1.42 ± 0.25	0.020	1.11 ± 0.57	0.65	0.39 ± 0.18	0.00098
Motionless % time	0.41 ± 0.15	0.0024	1.08 ± 0.49	0.0063	0.63 ± 0.2	0.0078	1.43 ± 0.53	0.060	0.5 ± 0.19	0.020	0.18 ± 0.1	0.0039	2.84 ± 0.34	0.00098
Locomotion duration [b]	1.83 ± 0.36	0.00049	0.91 ± 0.05	**0.000031**	1.38 ± 0.17	0.0078	0.57 ± 0.08	**0.000015**	1.58 ± 0.21	0.0020	1.7 ± 0.41	0.0039	0.95 ± 0.23	0.21
Fine movement duration	0.96 ± 0.03	0.016	1.01 ± 0.06	0.011	0.94 ± 0.04	0.039	1.16 ± 0.1	0.0010	0.85 ± 0.08	0.0098	0.93 ± 0.07	0.027	0.94 ± 0.05	0.019
Rearing duration	1.17 ± 0.13	0.11	0.99 ± 0.11	0.074	1.34 ± 0.49	0.31	0.7 ± 0.12	0.0066	0.92 ± 0.12	0.16	0.84 ± 0.29	0.82	1.28 ± 0.56	0.43
Motionless duration	0.78 ± 0.1	0.0093	0.95 ± 0.09	0.86	0.95 ± 0.13	0.38	0.88 ± 0.11	0.067	1.0 ± 0.28	0.63	0.61 ± 0.08	0.0039	1.67 ± 0.32	0.0020
Locomotion-fine movement frequency	0.77 ± 0.14	0.00049	1.08 ± 0.08	**0.000061**	0.79 ± 0.17	0.039	1.32 ± 0.26	0.00033	0.62 ± 0.04	0.0020	1.01 ± 0.24	0.50	0.72 ± 0.13	0.0020
Locomotion-rearing frequency	1.02 ± 0.13	0.93	1.0 ± 0.18	0.75	0.87 ± 0.11	0.054	0.76 ± 0.11	0.083	1.43 ± 0.07	0.0020	1.14 ± 0.13	0.31	0.57 ± 0.29	0.031
Locomotion-motionless frequency	0.7 ± 0.21	0.034	1.06 ± 0.31	0.021	0.88 ± 0.25	0.64	1.37 ± 0.35	0.0019	0.73 ± 0.21	0.29	0.77 ± 0.06	0.0039	1.38 ± 0.35	0.0088
Fine movement-locomotion frequency	0.77 ± 0.11	0.00049	1.06 ± 0.11	**0.00015**	0.79 ± 0.16	0.039	1.35 ± 0.24	**0.00011**	0.64 ± 0.08	0.0020	1.02 ± 0.3	0.48	0.8 ± 0.12	0.0020
Fine movement-rearing frequency	0.95 ± 0.08	0.12	1.0 ± 0.22	0.39	0.99 ± 0.08	> 0.99	0.96 ± 0.16	0.54	0.97 ± 0.2	0.47	0.86 ± 0.46	0.44	0.0 ± 0.0	> 0.99
Fine movement-motionless frequency	0.71 ± 0.15	0.034	1.06 ± 0.2	0.034	0.72 ± 0.12	0.078	1.31 ± 0.36	0.048	0.6 ± 0.11	0.063	0.45 ± 0.11	0.0039	1.56 ± 0.36	0.00098
Rearing-locomotion frequency	1.09 ± 0.16	0.83	1.03 ± 0.18	0.9	0.95 ± 0.16	0.74	0.81 ± 0.19	0.086	1.17 ± 0.06	0.027	1.07 ± 0.18	0.81	0.67 ± 0.17	0.0078
Rearing-fine movement frequency	1.0 ± 0.0	0.25	1.0 ± 0.15	0.57	0.95 ± 0.06	0.13	0.9 ± 0.13	0.49	0.78 ± 0.28	0.13	1.0 ± 0.14	0.63	1.0 ± 0.33	> 0.99
Motionless-locomotion frequency	0.71 ± 0.13	0.077	1.01 ± 0.33	0.0082	0.92 ± 0.17	0.74	1.31 ± 0.33	0.054	0.78 ± 0.13	0.027	0.71 ± 0.07	0.0078	1.42 ± 0.27	0.0059
Motionless-fine movement frequency	0.72 ± 0.12	0.027	0.96 ± 0.39	0.074	0.71 ± 0.09	0.023	1.36 ± 0.25	0.027	0.72 ± 0.31	0.29	0.43 ± 0.11	0.0039	1.67 ± 0.35	0.00098

Footnotes: [a] Unit for all frequencies is count/10 s. [b] Unit for all durations is seconds. [c] Wilcoxon test; two-tailed exact P values are shown. The bolded P values are significant when using a Bonferroni correction at a significance level of 0.05

Table 4. Properties of spontaneous IPSCs in PV⁺ neurons and Npas1⁺ neurons

		PV⁺ neurons		Npas1⁺ neurons		Mann–Whitney[b]
		Median ± MAD	n[a]	Median ± MAD	n	
All spontaneous inhibitory postsynaptic currents [c]	Rate (/s)	12.89 ± 3.63	50	7.76 ± 2.90	47	0.025
	Amplitude (pA)	71.00 ± 20.54	50	60.24 ± 13.11	47	0.037
Autocorrelation fit parameters	Aperiodic rate (/s)	8.01 ± 3.13	12	7.37 ± 1.34	10	> 0.99
	Presynaptic frequency (/s)	8.88 ± 2.03	13	9.75 ± 1.14	11	0.49
	Periodic rate (/s)	6.69 ± 1.17	13	7.25 ± 1.50	11	0.56
	Presynaptic CV(ISI)	0.13 ± 0.04	13	0.15 ± 0.06	11	0.28
	Power parameter	0.70 ± 0.23	13	0.72 ± 0.10	11	0.88
Unitary inhibitory postsynaptic currents	Amplitude (pA)	133.64 ± 71.95	12	82.70 ± 40.25	10	0.20
	CV	0.50 ± 0.16	12	0.56 ± 0.10	10	0.54
	Amplitude with failures (pA)	111.91 ± 68.80	12	72.86 ± 39.60	10	0.25
	CV with failures	0.80 ± 0.34	12	0.85 ± 0.11	10	0.82
	Var/mean with failures	79.00 ± 11.15	12	34.36 ± 10.50	10	0.15

[a] n equal to the number of neurons. [b] Two-tailed exact P values are listed. The bolded p values are considered significant (< 0.05).
[c] Both rate and amplitude are not significant after correction for multiple testing.

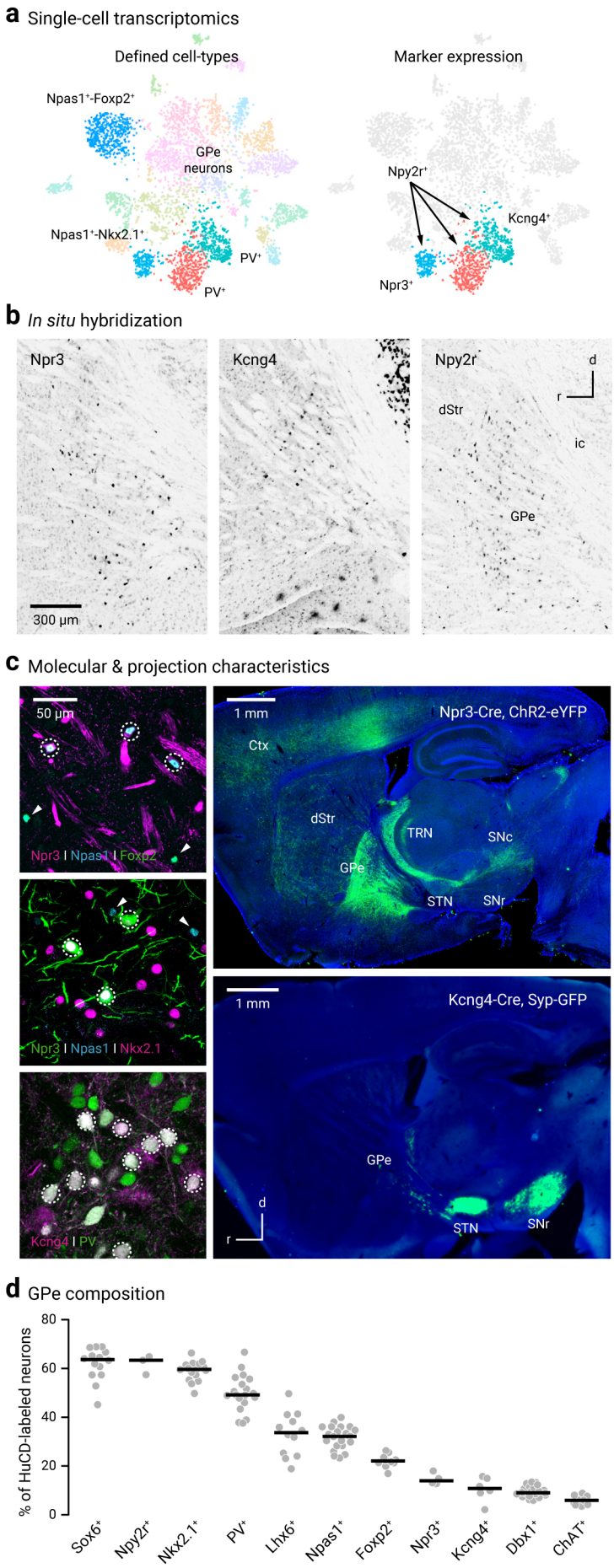
a Single-cell transcriptomics
Defined cell-types
Marker expression
Npas1+-Foxp2+
GPe neurons
Npas1+-Nkx2.1+
PV+
PV+
Npy2r+
Kcng4+
Npr3+
b In situ hybridization
Npr3
Kcng4
Npy2r
d
r
dStr
ic
GPe
300 µm
c Molecular & projection characteristics
50 µm
Npr3 I Npas1 I Foxp2
Npr3 I Npas1 I Nkx2.1
Kcng4 I PV
1 mm
Npr3-Cre, ChR2-eYFP
Ctx
dStr
TRN
SNc
GPe
STN
SNr
1 mm
Kcng4-Cre, Syp-GFP
GPe
d
r
STN
SNr
d GPe composition
% of HuCD-labeled neurons
80
60
40
20
0
Sox6+
Npy2r+
Nkx2.1+
PV+
Lhx6+
Npas1+
Foxp2+
Npr3+
Kcng4+
Dbx1+
ChAT+

Figure 1

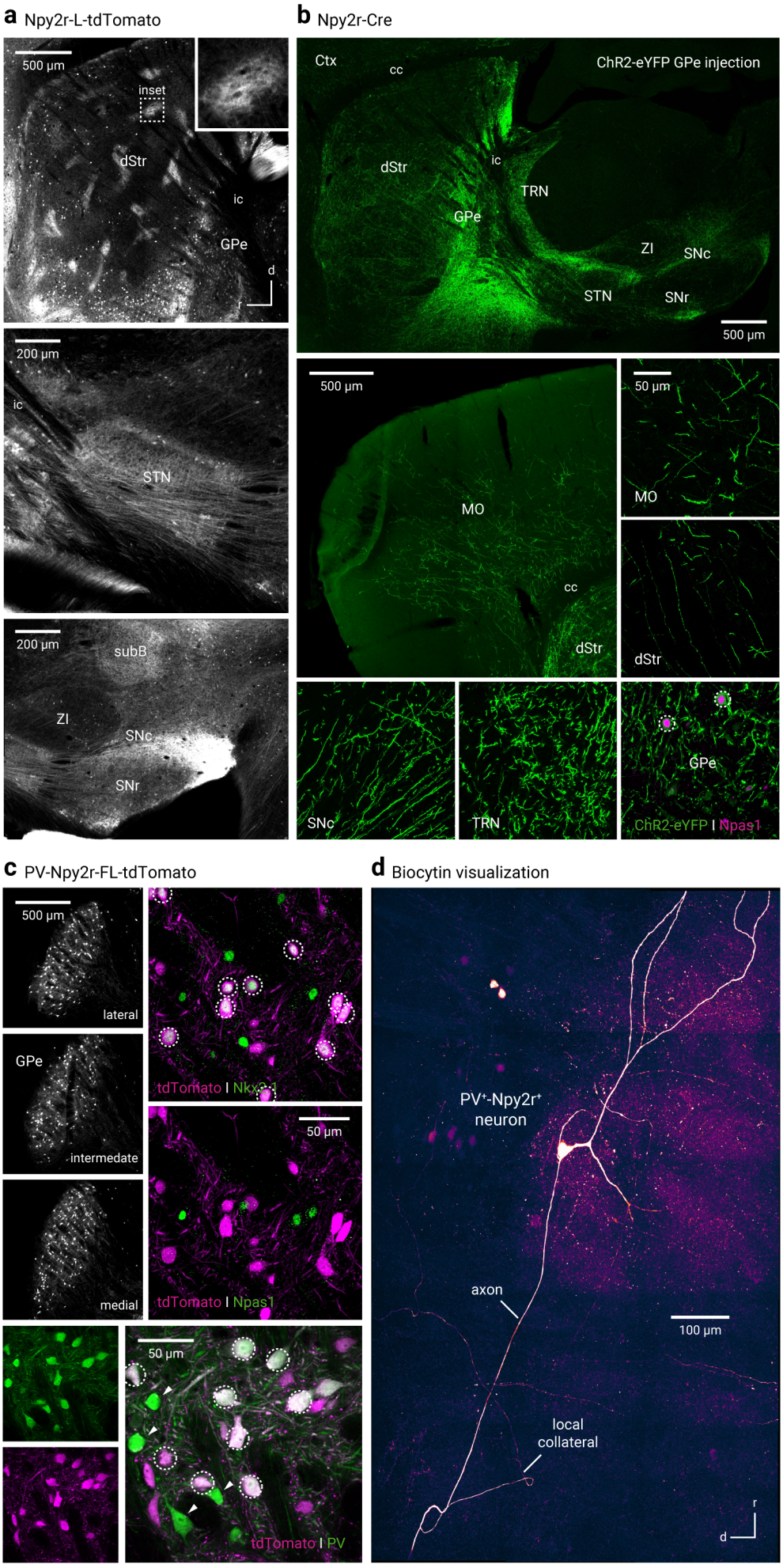
a Npy2r-L-tdTomato
500 µm
inset
dStr
ic
GPe
d
r
200 µm
ic
STN
200 µm
subB
ZI
SNc
SNr
b Npy2r-Cre
Ctx
cc
ChR2-eYFP GPe injection
dStr
ic
TRN
GPe
ZI
SNc
STN
SNr
500 µm
500 µm
MO
cc
dStr
50 µm
MO
dStr
SNc
TRN
GPe
ChR2-eYFP | Npas1
c PV-Npy2r-FL-tdTomato
500 µm
lateral
GPe
intermedate
medial
tdTomato | Nkx2-1
50 µm
tdTomato | Npas1
50 µm
tdTomato | PV
d Biocytin visualization
PV+-Npy2r+
neuron
axon
100 µm
local
collateral
r
d

Figure 2

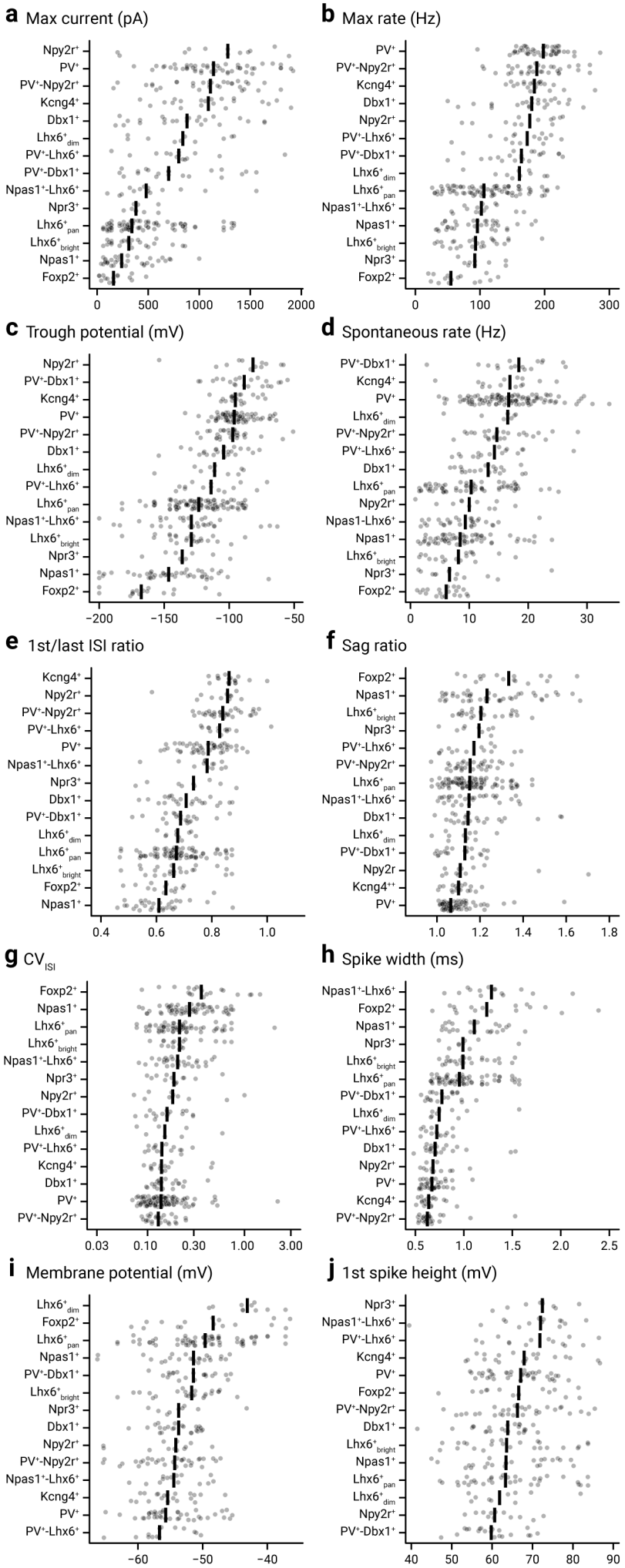
a Max current (pA)
Npy2r+
PV+
PV+-Npy2r+
Kcng4+
Dbx1+
Lhx6+dim
PV+-Lhx6+
PV+-Dbx1+
Npas1+-Lhx6+
Npr3+
Lhx6+pan
Lhx6+bright
Npas1+
Foxp2+
0 500 1000 1500 2000
b Max rate (Hz)
PV+
PV+-Npy2r+
Kcng4+
Dbx1+
Npy2r+
PV+-Lhx6+
PV+-Dbx1+
Lhx6+dim
Lhx6+pan
Npas1+-Lhx6+
Npas1+
Lhx6+bright
Npr3+
Foxp2+
0 100 200 300
c Trough potential (mV)
Npy2r+
PV+-Dbx1+
Kcng4+
PV+
PV+-Npy2r+
Dbx1+
Lhx6+dim
PV+-Lhx6+
Lhx6+pan
Npas1+-Lhx6+
Lhx6+bright
Npr3+
Npas1+
Foxp2+
−200 −150 −100 −50
d Spontaneous rate (Hz)
PV+-Dbx1+
Kcng4+
PV+
Lhx6+dim
PV+-Npy2r+
PV+-Lhx6+
Dbx1+
Lhx6+pan
Npy2r+
Npas1-Lhx6+
Npas1+
Lhx6+bright
Npr3+
Foxp2+
0 10 20 30
e 1st/last ISI ratio
Kcng4+
Npy2r+
PV+-Npy2r+
PV+-Lhx6+
PV+
Npas1+-Lhx6+
Npr3+
Dbx1+
PV+-Dbx1+
Lhx6+dim
Lhx6+pan
Lhx6+bright
Foxp2+
Npas1+
0.4 0.6 0.8 1.0
f Sag ratio
Foxp2+
Npas1+
Lhx6+bright
Npr3+
PV+-Lhx6+
PV+-Npy2r+
Lhx6+pan
Npas1+-Lhx6+
Dbx1+
Lhx6+dim
PV+-Dbx1+
Npy2r
Kcng4++
PV+
1.0 1.2 1.4 1.6 1.8
g CVISI
Foxp2+
Npas1+
Lhx6+pan
Lhx6+bright
Npas1+-Lhx6+
Npr3+
Npy2r+
PV+-Dbx1+
Lhx6+dim
PV+-Lhx6+
Kcng4+
Dbx1+
PV+
PV+-Npy2r+
0.03 0.10 0.30 1.00 3.00
h Spike width (ms)
Npas1+-Lhx6+
Foxp2+
Npas1+
Npr3+
Lhx6+bright
Lhx6+pan
PV+-Dbx1+
Lhx6+dim
PV+-Lhx6+
Dbx1+
Npy2r+
PV+
Kcng4+
PV+-Npy2r+
0.5 1.0 1.5 2.0 2.5
i Membrane potential (mV)
Lhx6+dim
Foxp2+
Lhx6+pan
Npas1+
PV+-Dbx1+
Lhx6+bright
Npr3+
Dbx1+
Npy2r+
PV+-Npy2r+
Npas1+-Lhx6+
Kcng4+
PV+
PV+-Lhx6+
−60 −50 −40
j 1st spike height (mV)
Npr3+
Npas1+-Lhx6+
PV+-Lhx6+
Kcng4+
PV+
Foxp2+
PV+-Npy2r+
Dbx1+
Lhx6+bright
Npas1+
Lhx6+pan
Lhx6+dim
Npy2r+
PV+-Dbx1+
40 50 60 70 80 90

Figure 3

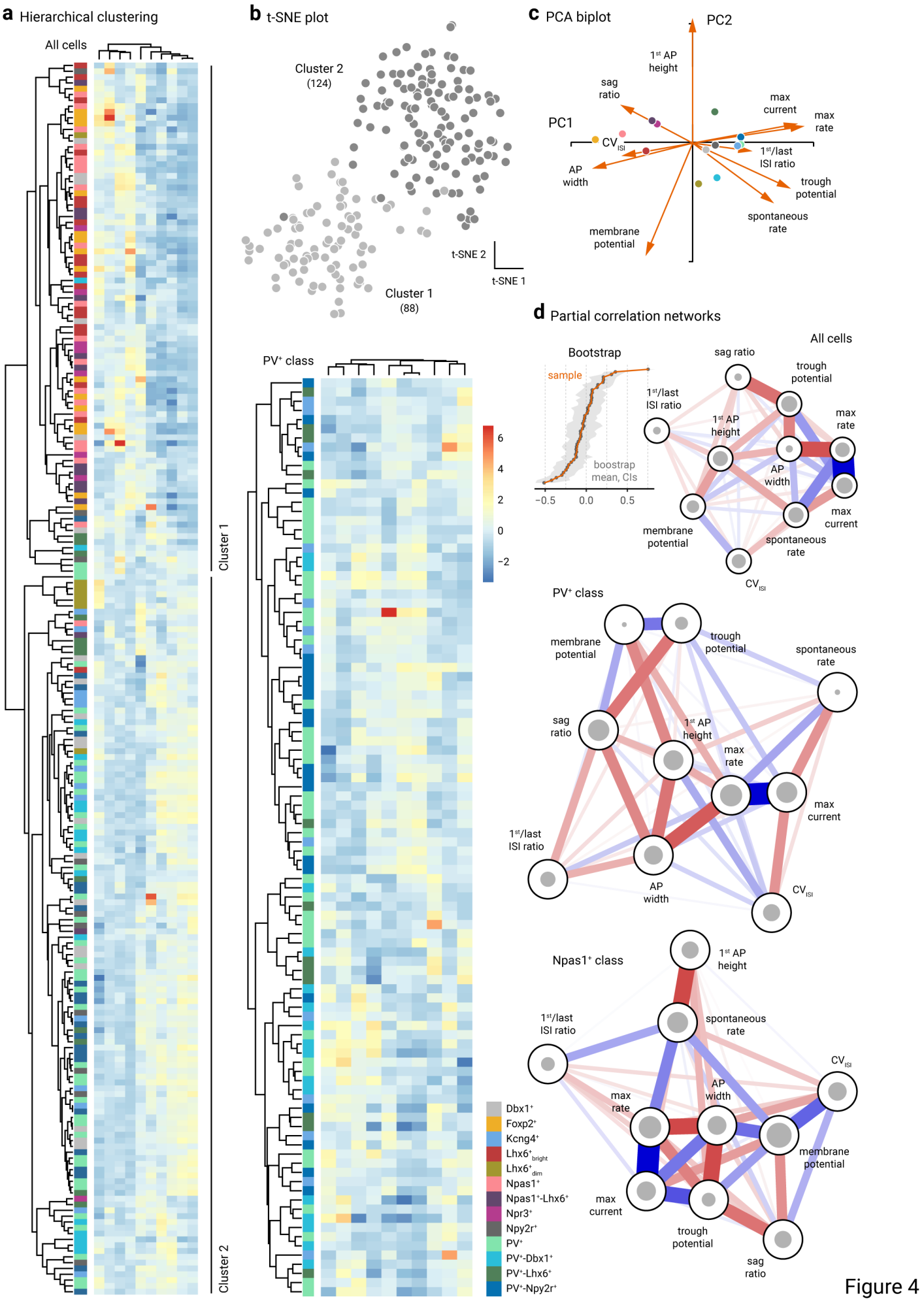
a Hierarchical clustering
All cells
Cluster 1
Cluster 2
b t-SNE plot
Cluster 2
(124)
Cluster 1
(88)
t-SNE 2
t-SNE 1
c PCA biplot
PC2
PC1
1st AP height
sag ratio
max current
max rate
CVISI
1st/last ISI ratio
AP width
trough potential
spontaneous rate
membrane potential
d Partial correlation networks
Bootstrap
sample
boostrap mean, CIs
−0.5
0.0
0.5
All cells
PV+ class
Npas1+ class
6
4
2
0
−2
Dbx1+
Foxp2+
Kcng4+
Lhx6+bright
Lhx6+dim
Npas1+
Npas1+-Lhx6+
Npr3+
Npy2r+
PV+
PV+-Dbx1+
PV+-Lhx6+
PV+-Npy2r+

Figure 4

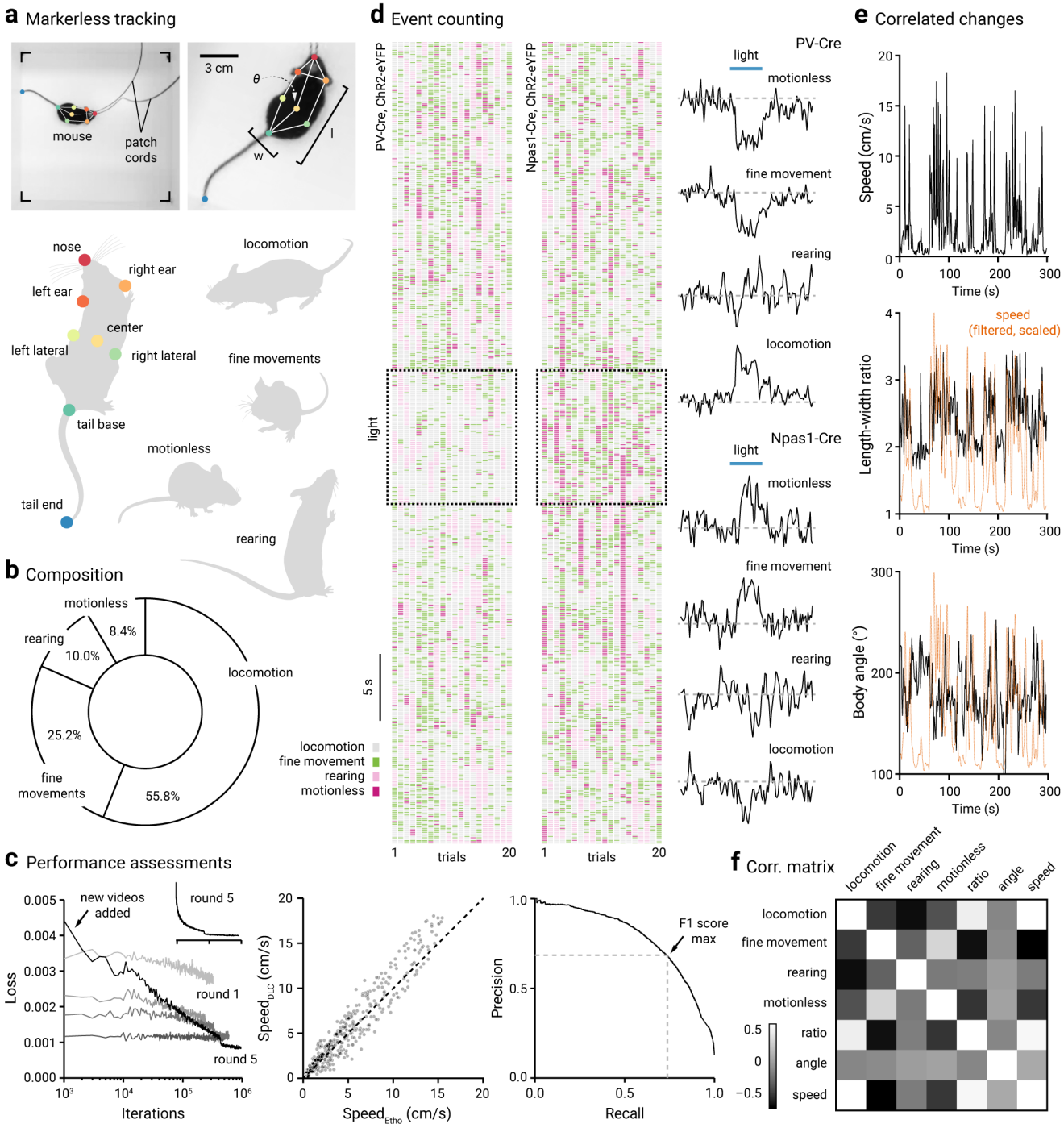
a Markerless tracking
mouse
patch cords
3 cm
θ
w
l
nose
right ear
left ear
center
left lateral
right lateral
tail base
tail end
locomotion
fine movements
motionless
rearing
b Composition
motionless
8.4%
rearing
10.0%
locomotion
25.2%
fine movements
55.8%
locomotion
fine movement
rearing
motionless
c Performance assessments
new videos added
round 5
round 1
round 5
Loss
Iterations
Speed$_{DLC}$ (cm/s)
Speed$_{Etho}$ (cm/s)
Precision
Recall
F1 score max
d Event counting
PV-Cre, ChR2-eYFP
Npas1-Cre, ChR2-eYFP
light
5 s
trials
PV-Cre
Npas1-Cre
e Correlated changes
Speed (cm/s)
Time (s)
speed (filtered, scaled)
Length-width ratio
Body angle (°)
f Corr. matrix
locomotion
fine movement
rearing
motionless
ratio
angle
speed

Figure 5

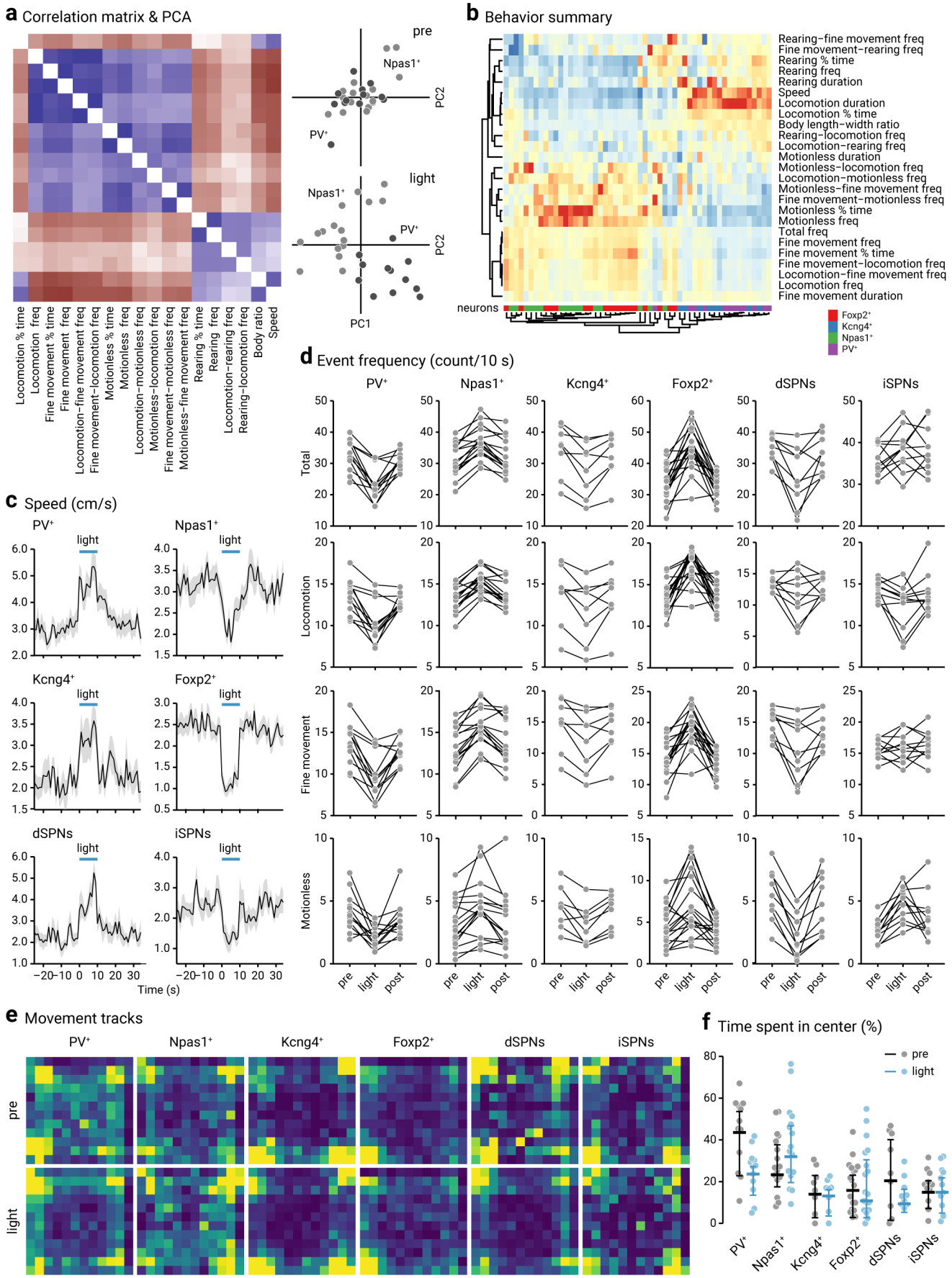
a Correlation matrix & PCA
Locomotion % time
Locomotion freq
Fine movement % time
Fine movement freq
Locomotion−fine movement freq
Fine movement−locomotion freq
Motionless % time
Motionless freq
Locomotion−motionless freq
Motionless−locomotion freq
Fine movement−motionless freq
Motionless−fine movement freq
Rearing % time
Rearing freq
Locomotion−rearing freq
Rearing−locomotion freq
Body ratio
Speed
pre
light
PC1
PC2
Npas1+
PV+
b Behavior summary
Rearing−fine movement freq
Fine movement−rearing freq
Rearing % time
Rearing freq
Rearing duration
Speed
Locomotion duration
Locomotion % time
Body length−width ratio
Rearing−locomotion freq
Locomotion−rearing freq
Motionless duration
Motionless−locomotion freq
Locomotion−motionless freq
Motionless−fine movement freq
Fine movement−motionless freq
Motionless % time
Motionless freq
Total freq
Fine movement freq
Fine movement % time
Fine movement−locomotion freq
Locomotion−fine movement freq
Locomotion freq
Fine movement duration
neurons
Foxp2+
Kcng4+
Npas1+
PV+
c Speed (cm/s)
PV+
Npas1+
Kcng4+
Foxp2+
dSPNs
iSPNs
light
Time (s)
d Event frequency (count/10 s)
PV+
Npas1+
Kcng4+
Foxp2+
dSPNs
iSPNs
Total
Locomotion
Fine movement
Motionless
pre
light
post
e Movement tracks
PV+
Npas1+
Kcng4+
Foxp2+
dSPNs
iSPNs
pre
light
f Time spent in center (%)
pre
light
PV+
Npas1+
Kcng4+
Foxp2+
dSPNs
iSPNs

Figure 6

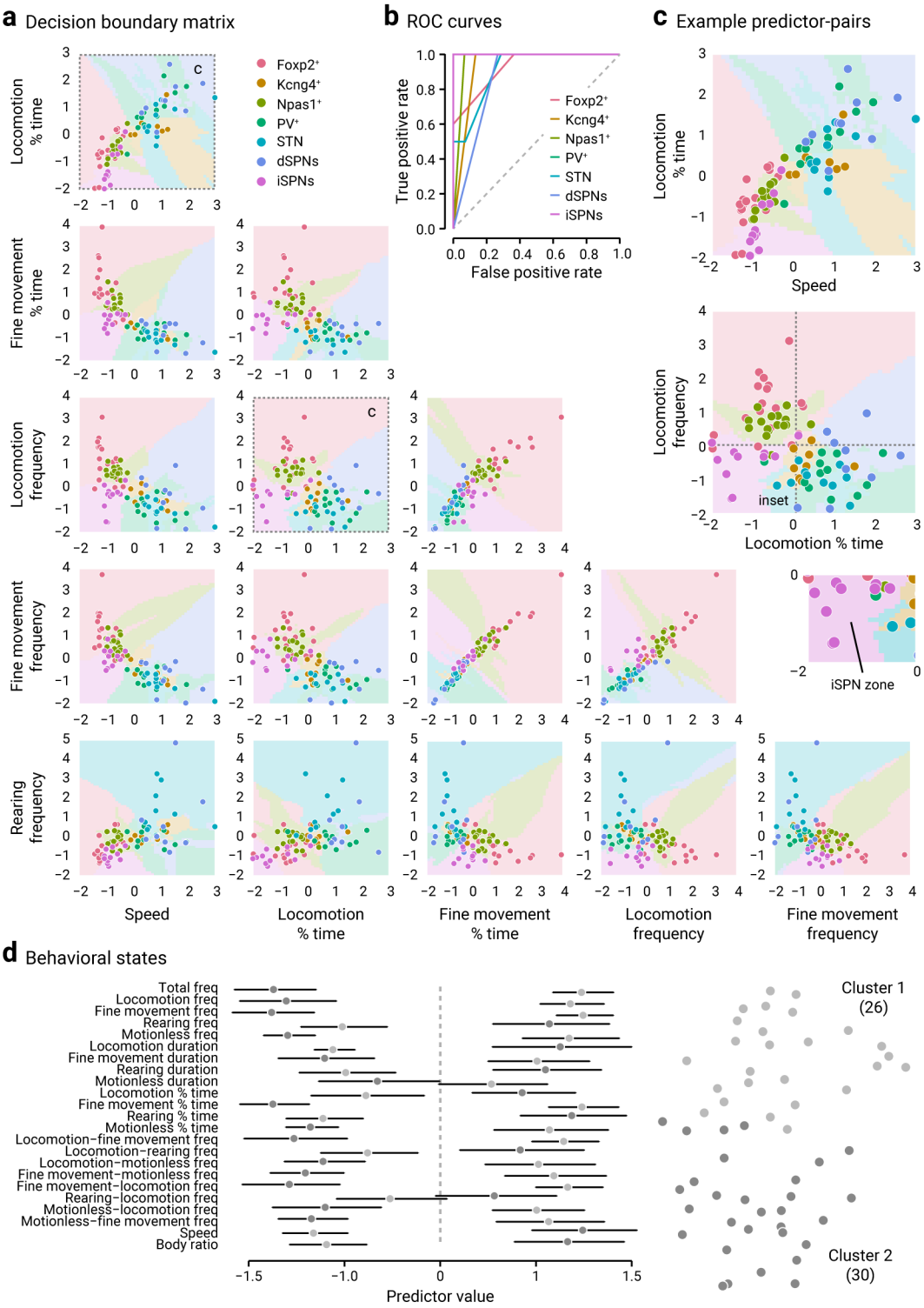
a Decision boundary matrix
b ROC curves
c Example predictor-pairs
d Behavioral states
Foxp2+
Kcng4+
Npas1+
PV+
STN
dSPNs
iSPNs
True positive rate
False positive rate
Locomotion % time
Fine movement % time
Locomotion frequency
Fine movement frequency
Rearing frequency
Speed
Locomotion % time
Fine movement % time
Locomotion frequency
Fine movement frequency
inset
iSPN zone
Total freq
Locomotion freq
Fine movement freq
Rearing freq
Motionless freq
Locomotion duration
Fine movement duration
Rearing duration
Motionless duration
Locomotion % time
Fine movement % time
Rearing % time
Motionless % time
Locomotion–fine movement freq
Locomotion–rearing freq
Locomotion–motionless freq
Fine movement–motionless freq
Fine movement–locomotion freq
Rearing–locomotion freq
Motionless–locomotion freq
Motionless–fine movement freq
Speed
Body ratio
Predictor value
Cluster 1
(26)
Cluster 2
(30)

Figure 7

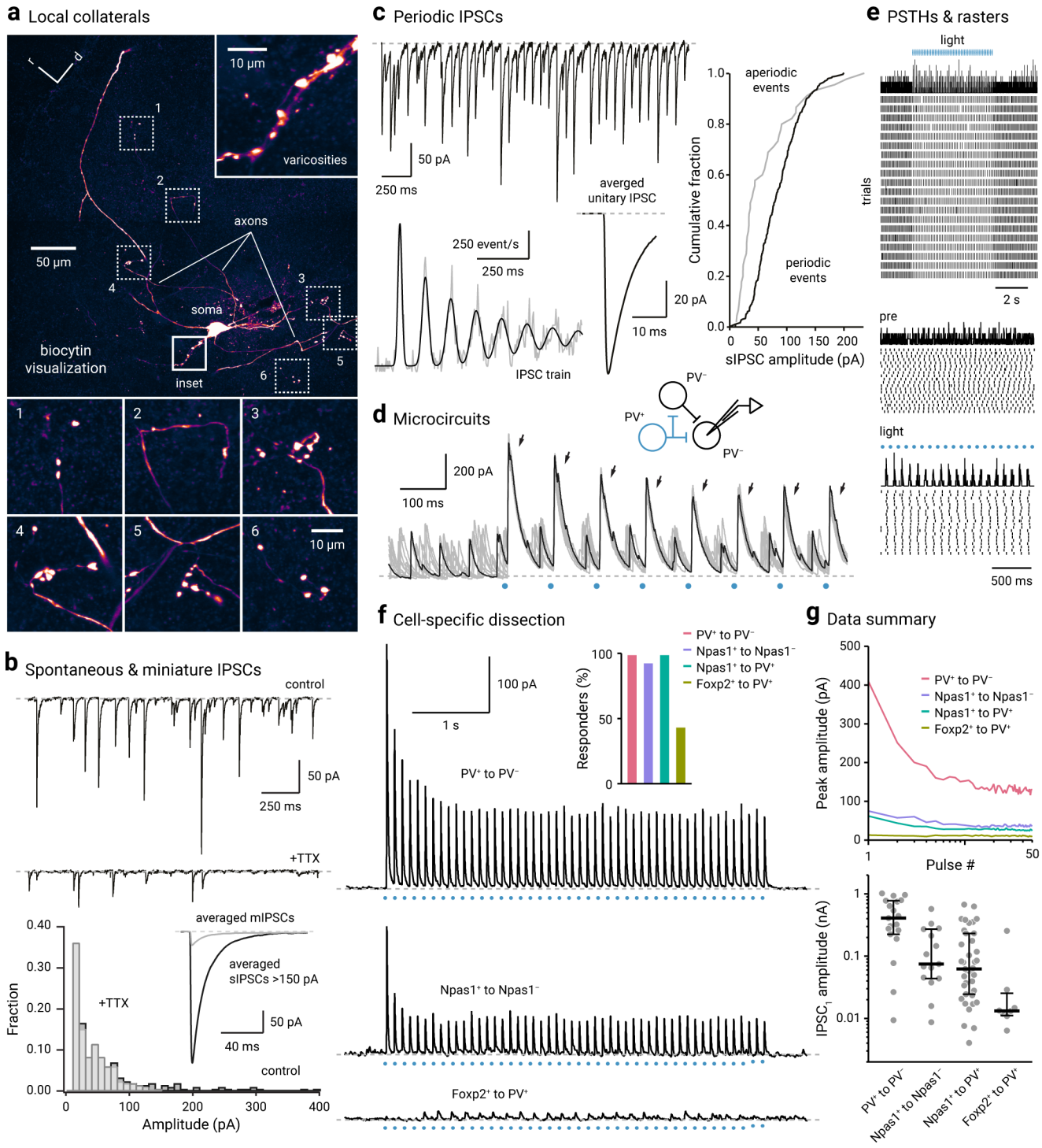
a Local collaterals
10 µm
varicosities
axons
50 µm
soma
biocytin visualization
inset
10 µm
b Spontaneous & miniature IPSCs
control
50 pA
250 ms
+TTX
averaged mIPSCs
averaged sIPSCs >150 pA
50 pA
40 ms
control
+TTX
Fraction
Amplitude (pA)
c Periodic IPSCs
50 pA
250 ms
averged unitary IPSC
250 event/s
250 ms
20 pA
10 ms
IPSC train
aperiodic events
periodic events
Cumulative fraction
sIPSC amplitude (pA)
d Microcircuits
PV⁺
PV⁻
PV⁻
200 pA
100 ms
e PSTHs & rasters
light
trials
2 s
pre
light
500 ms
f Cell-specific dissection
100 pA
1 s
PV⁺ to PV⁻
Npas1⁺ to Npas1⁻
Npas1⁺ to PV⁺
Foxp2⁺ to PV⁺
Responders (%)
g Data summary
PV⁺ to PV⁻
Npas1⁺ to Npas1⁻
Npas1⁺ to PV⁺
Foxp2⁺ to PV⁺
Peak amplitude (pA)
Pulse #
IPSC1 amplitude (nA)

Figure 8